

# Impact of Graupel Parameterization Schemes on Idealized Bow Echo Simulations

REBECCA D. ADAMS-SELIN

*Atmospheric and Environmental Research, Inc., Lexington, Massachusetts, and Department of Atmospheric Science,  
Colorado State University, Fort Collins, Colorado*

SUSAN C. VAN DEN HEEVER AND RICHARD H. JOHNSON

*Department of Atmospheric Science, Colorado State University, Fort Collins, Colorado*

(Manuscript received 24 February 2012, in final form 10 October 2012)

## ABSTRACT

The effect of changes in microphysical cooling rates on bow echo development and longevity are examined through changes to graupel parameterization in the Advanced Research Weather Research and Forecasting Model (ARW-WRF). Multiple simulations are performed that test the sensitivity to different graupel size distributions as well as the complete removal of graupel. It is found that size distributions with larger and denser, but fewer, graupel hydrometeors result in a weaker cold pool due to reduced microphysical cooling rates. This yields weaker midlevel (3–6 km) buoyancy and pressure perturbations, a later onset of more elevated rear inflow, and a weaker convective updraft. The convective updraft is also slower to tilt rearward, and thus bowing occurs later. Graupel size distributions with more numerous, smaller, and lighter hydrometeors result in larger microphysical cooling rates, stronger cold pools, more intense midlevel buoyancy and pressure gradients, and earlier onset of surface-based rear inflow; these systems develop bowing segments earlier. A sensitivity test with fast-falling but small graupel hydrometeors revealed that small mean size and slow fall speed both contribute to the strong cooling rates. Simulations entirely without graupel are initially weaker, because of limited contributions from cooling by melting of the slowly falling snow. However, over the next hour increased rates of melting snow result in an increasingly more intense system with new bowing. Results of the study indicate that the development of a bow echo is highly sensitive to microphysical processes, which presents a challenge to the prediction of these severe weather phenomena.

## 1. Introduction

It is well known that a key component to the strength, structure, and longevity of bow echoes is the cold pool (Rotunno et al. 1988; Weisman 1992, 1993; Weisman and Rotunno 2005). Changes in the rates of cooling by microphysical processes have a large effect on the shape and strength of the cold pool (Lin et al. 1983; Fovell and Ogura 1988; James et al. 2006), and hence the eventual storm structure, longevity, and development. While the impact of microphysical scheme variations on cold pool and storm structure have been noted for supercells (Gilmore et al. 2004a; van den Heever and Cotton 2004, 2007; Dawson et al. 2010; Snook and Xue 2008; Lerach

et al. 2008) and squall lines (Nicholls 1987; Tao and Simpson 1989; Fovell and Ogura 1988; Szeto and Cho 1994; Morrison et al. 2009; Bryan and Morrison 2012), few, if any, studies have looked at the effects on development and maintenance of bow echoes.

Multiple studies (Hane 1973; Thorpe et al. 1982; Nicholls et al. 1988; Rotunno et al. 1988) have noted a relationship between the tilt of the convective updraft and the balance between vorticities generated at the front edge of the cold pool and by the environmental wind. When these two vorticity sources are balanced, the convective updraft remains upright, and stronger, by virtue of low-level air being lifted into the upper levels over a shorter distance. This does not necessarily translate to system longevity (Fovell and Ogura 1989; Lafore and Moncrieff 1989) but has been related to system intensity (Rotunno et al. 1988; Weisman and Rotunno 2004; Bryan et al. 2006; Parker 2010), although some studies question even that (Stensrud et al. 2005). When

---

*Corresponding author address:* Rebecca D. Adams-Selin, HQ Air Force Weather Agency 16th Weather Squadron, 101 Nelson Dr., Offutt AFB, NE 68113.  
E-mail: rebecca.selin.ctr@offutt.af.mil

the cold pool and its associated vorticity strengthens, the updraft tilts rearward over the cold pool (Rotunno et al. 1988). The buoyancy gradient between it and the warm outflow from the updraft aloft increases, resulting in a strengthened midlevel low pressure perturbation (Garner and Thorpe 1992; Weisman and Rotunno 2005).

Lafore and Moncrieff (1989) and Weisman (1992) found that rear-to-front flow, or the rear-inflow jet, in the system at mid- and low levels forms in response to this midlevel buoyancy and pressure gradient; more recent studies have found this flow to be generated by a rearward-propagating gravity wave generated by low-level microphysical cooling (Pandya and Durran 1996; Pandya et al. 2000). Given a large stratiform region or intense cold pool, the rear-inflow jet descends to the surface gradually, farther behind the convective line (Weisman 1992); the farther the microphysical cooling extends behind the convective line, the farther rearward the rear inflow descends to the surface (Pandya and Durran 1996; Pandya et al. 2000). As a result the positive vorticity source associated with the back bottom edge of the cold pool is minimal, and the updraft is allowed to tilt farther rearward over the cold pool. Systems in which the rear inflow is largely surface based are expected to develop more quickly and create bowing segments, but are not anticipated to be as long lived (Weisman 1993). Conversely, systems with elevated rear inflow generate additional positive vorticity that can balance the negative vorticity generated by the cold pool, aiding a more upright updraft (Weisman 1992).

A temporary, local intensification of the cold pool and its associated vorticity can result in only a portion of the storm updraft temporarily tilting farther upshear (Lafore and Moncrieff 1989; Weisman 1993; Weisman and Rotunno 2005; James et al. 2006). This additional tilt allows horizontal momentum within the system rear-to-front flow to be more easily transported to the surface, resulting in damaging downburst winds. These winds enhance evaporation by entraining additional unsaturated air, further cooling the cold pool. The combination of additional horizontal momentum and a more intense cold pool acts to locally increase the speed of the convective line, resulting in development of a bowing segment within the convective line (Weisman 1993; Weisman and Rotunno 2005; James et al. 2006).

Naturally, changes in the microphysical characteristics, through changes in heating and cooling rates, can have a large effect on the cold pool and resulting vorticity balances. The importance of the inclusion of ice in convective squall-line simulations has been noted multiple times in the literature: the additional intensification of the updraft due to latent heat from freezing is required to best simulate the updraft strength and resultant system

front-to-rear flow (Nicholls 1987; Tao and Simpson 1989; Fovell and Ogura 1988; Szeto and Cho 1994). Simulations that include ice have a larger and more realistic stratiform precipitation structure (Fovell and Ogura 1988). Cooling by melting also contributes significantly to the cold pool strength, and hence the midlevel thermal and pressure gradients in the stratiform region (Chen and Cotton 1988; Szeto and Cho 1994). This also enhances the speed of the rear-inflow jet. Yang and Houze (1995) performed a simulation that included a hail parameter, in addition to cloud ice. They noted a much narrower stratiform precipitation region, weaker midlevel buoyancy and pressure perturbation, and resulting weaker rear-inflow jet with the inclusion of hail.

Multiple studies have been performed examining the effects of using graupel or hail as the rimed frozen species in addition to snow and cloud ice. In Bryan and Morrison (2012), a hail squall-line simulation produced a much narrower convective line with higher simulated reflectivities and a slightly smaller stratiform region, compared to the graupel simulation. Seigel and van den Heever (2013) noted increased rear-to-front and front-to-rear flows in simulations with smaller, less dense hail. van den Heever and Cotton (2004) and Cohen and McCaul (2006) found simulations with larger, denser hail resulted in weaker cold pools due to decreased evaporation and melting from hydrometeors with a faster fall speed and reduced surface area to volume ratio. Conversely, van Weverberg et al. (2011, 2012b) and Morrison and Milbrandt (2011) found the opposite: because of the faster hail fall speed, the downward precipitation flux was higher and consequentially the melting rate larger. Melting also extended to the surface instead of being confined to just below the melting level; this created a stronger surface cold pool. Gilmore et al. (2004a) found these results may be time dependent—their more graupel-like simulations' cold pools became coldest only late in the 2-h simulation; van Weverberg et al. (2012a) noted a dependency on updraft strength.

Changes in simulated microphysical heating and cooling rates can also be affected by the use of a one- or two-moment microphysics scheme. In a one-moment scheme, only one distribution variable can be explicitly predicted; this is almost always the hydrometeor mixing ratio. In a two-moment scheme, typically the hydrometeor mixing ratio and number concentration are prognostic. Multiple studies evaluating the differences between these schemes in both squall-line and supercell simulations have been performed; these studies also note the large effects changes in the heating and cooling profile of a system can have (Morrison et al. 2009; Dawson et al. 2010; Bryan and Morrison 2012; van Weverberg et al.

2012b). Through the variation in particle number concentration allowed by the double-moment scheme, particularly that of rain and graupel (van Weverberg et al. 2012b), evaporation rates were reduced because of changes in the total particle surface area, resulting in a weaker system cold pool. Within squall lines, this effect was largely evident in the stratiform region (Bryan and Morrison 2012).

Thus, variations in the ice parameters of a microphysical parameterization scheme can have large effects on system heating and cooling profiles and cold pool strength, among other factors. Additionally, cold pool strength and rear inflow play a large role in new bowing development. To this point, however, there have been no studies linking new bowing development to variations in microphysics schemes. Therefore, a cloud-resolving model is used to examine the impacts of microphysics specifically on bow echoes. The sensitivity of new bowing frequency and intensity to changes in microphysical heating and cooling rates will be investigated, particularly through their relation to cold pool strength and depth, rear-to-front flow within the system, and the stratiform region microphysical structure.

Section 2 describes the experiment and model design, as well as the specific microphysics variations. Sections 3 and 4 contain results from the two different sensitivity studies performed, and section 5 presents the conclusions.

## 2. Methodology

### a. Model description

The Advanced Research Weather Research and Forecasting Model (ARW-WRF) is widely recognized as a reliable tool for simulations of mesoscale phenomena (Skamarock et al. 2008). Here, version 3.2.1 was used to simulate a bow echo case over Oklahoma. The model horizontal grid spacing was 1 km, with 72 stretched vertical levels. In total, the domain extended 600 km in the  $x$  direction, 400 km in the  $y$  direction, and to 100 hPa vertically. Rayleigh damping was applied over the top 5 km of the atmosphere, with a damping coefficient of 0.003. The  $x$  and  $y$  boundaries were open, and no random perturbations were utilized. No convective, boundary layer, radiative, or land surface parameterizations were used. A 1.5-order turbulent kinetic energy (TKE) closure turbulence parameterization was selected. No surface friction was applied within the model, as in the Weisman (1992, 1993) studies; surface wind speeds and gravity current propagation will be somewhat faster than expected.

The 0000 UTC 13 March 2003 Norman, Oklahoma (KOUN), sounding (Fig. 1) provided the homogenous initial conditions. This sounding was chosen from among

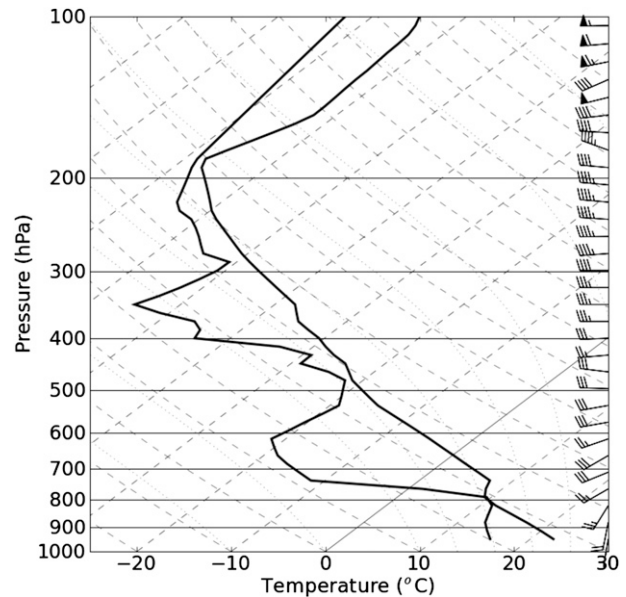


FIG. 1. 0000 UTC 13 Mar 2003 KOUN sounding, modified for use in the idealized simulations.

multiple case study simulations after tests showed a strong sensitivity of the bow to microphysics changes. This sensitivity is likely due to relatively weak line-normal wind shear for this modified sounding, with a large surface-based convective available potential energy (CAPE),  $3752 \text{ J kg}^{-1}$ . The low-level 0–2.5-km shear was  $14 \text{ m s}^{-1}$  and the 0–5-km layer shear was  $14.2 \text{ m s}^{-1}$ . The convective inhibition (CIN) was just  $6 \text{ J kg}^{-1}$ .

Other than extrapolation of moisture data at upper levels and minimal cooling to remove unstable layers, the sounding was unmodified. (The unstable layers were removed from the base-state sounding to prevent convective overturning immediately upon simulation start.) The observed convection formed along a southwest–northeast line approximately  $60^\circ$  clockwise of vertical. The sounding was not rotated in the idealized simulation, and the idealized convection was initiated along a south–north line. The line-normal wind shear values given above are for this idealized convection.

The simulations were run for 6 h. The “cold pool-dam break” initialization scheme, used by Weisman et al. (1997), was modified for these simulations. A “cold dam” of air was created by decreasing the initial potential temperature in the domain, from 0–200 km in the  $x$  direction and 50–350 km in the  $y$  direction. The magnitude of the perturbation was 6 K at the surface, and linearly decreased until reaching 0 K, 2.5 km aloft. Upon simulation start, the “dam” of cold air would break, surging forward as a gravity current. Air in advance of

the gravity current would be forced upward, initiating convective activity. This initialization method was specifically chosen because of the low-level stable layer in the initial sounding (Fig. 1). This stable layer acted as a cap and required a larger amount of forcing to be overcome than would be provided by a warm bubble initialization. In every simulation, cold pool perturbations significantly colder than the initial 6 K developed within 1 h; within 2 h negative perturbations of 10–14 K were common.

### b. Model microphysics and experiment design

A total of six sensitivity tests were performed using the WRF single-moment 5- and 6-class microphysics schemes (WSM5 and WSM6, respectively; Hong et al. 2004; Hong and Lim 2006; Lim and Hong 2010), with the goal of examining how modifying the graupel microphysics class affects bowing development.

These schemes are originally based upon the techniques used in Lin et al. (1983) and Rutledge and Hobbs (1983). The 5-class schemes contain explicit classes for water vapor, cloud water, raindrops, cloud ice, and snow; the 6-class schemes add graupel. All of these schemes utilize an inverse exponential Marshall–Palmer size distribution (Marshall and Palmer 1948) for rain, snow, and, for the 6-class scheme, graupel:

$$n_x(D_x)dD_x = n_{0x} \exp(-\lambda_x D_x) dD_x, \quad (1)$$

where  $x$  is the microphysics class,  $n_x(D_x)dD_x$  is the number of hydrometeors per cubic meter with diameters between  $D_x$  and  $D_x + dD_x$ ,  $n_{0x}$  is the distribution intercept, and  $\lambda_x$  is the slope. Within these schemes, the distribution intercept is set to a constant value. The slope is a diagnosed value, defined as

$$\lambda_x = \left( \frac{\pi \rho_x n_{0x}}{\rho q_x} \right)^{0.25}, \quad (2)$$

where  $\rho_x$  is the preassigned hydrometeor density ( $\text{kg m}^{-3}$ ),  $\rho$  ( $\text{kg m}^{-3}$ ) is the local air density, and  $q_x$  ( $\text{kg kg}^{-1}$ ) is the prognostic hydrometeor mixing ratio.

From (1) and (2), it can be seen that the size distribution of a hydrometeor is a function of  $n_{0x}$  and  $\lambda_x$ . Because of the inverse nature of the distribution, with all other factors held constant, a large intercept will result in a smaller mean hydrometeor size, and vice versa. In general, graupel hydrometeors have a smaller mean hydrometeor size (larger intercept) and are less dense, while hail stones have a larger mean hydrometeor size (smaller intercept) and are more dense, but there is quite a bit of overlap between the two in observed data. Gilmore et al. (2004a) provided an excellent summary of

previous observations of these values: the intercept value for hail and graupel ranged from  $10^2 \text{ m}^{-4}$  for large hail, to  $10^{10} \text{ m}^{-4}$  for extremely small graupel (Cheng et al. 1985; Dennis et al. 1971; Federer and Waldvogel 1975; Spahn 1976; Knight et al. 1982). Observations of graupel density ranged from 50 to  $890 \text{ kg m}^{-3}$ ; hail density varied from 700 to  $900 \text{ kg m}^{-3}$  (Pruppacher and Klett 1978).

In the first experiment, model runs are performed using the WSM6 scheme, but covering this observed range of intercept parameters and densities. The most “hail like” hydrometeor has an intercept equal to  $4 \times 10^2 \text{ m}^{-4}$  and a density of  $900 \text{ kg m}^{-3}$ ; the most “graupel like” hydrometeor an intercept of  $4 \times 10^6 \text{ m}^{-4}$  and a density of  $300 \text{ kg m}^{-3}$ ; and the “mid” simulation an intercept of  $4 \times 10^4 \text{ m}^{-4}$  and a density of  $700 \text{ kg m}^{-3}$ . A plot of the graupel hydrometeor size distributions given the chosen intercepts and densities is shown in Fig. 2a. A full list of the microphysical schemes and associated parameters used in each simulation is provided in Table 1.

Within these schemes, an increase in density alone acts to actually decrease the mass-weighted mean terminal velocity. This value is calculated for graupel through the following (Hong and Lim 2006):

$$v_g = \frac{a_g \Gamma(4 + b_g) \left( \frac{\rho_0}{\rho} \right)^{1/2}}{6} \frac{1}{\lambda_g^{b_g}}, \quad (3)$$

where  $a_g$  and  $b_g$  are empirically determined coefficients, set to 330 and 0.8, respectively, within the WSM6 scheme (Hong et al. 2009). An increase in graupel hydrometeor density with all other factors held constant results in an increased slope value through (2), yielding a smaller mean terminal velocity. This is different than the microphysics scheme used in Gilmore et al. (2004a), in which the fall speed was directly proportional to the hydrometeor density (Gilmore et al. 2004b). To account for this unphysical effect, the  $a_g$  empirical coefficient was modified slightly to negate the fall speed decrease caused by the density changes. A list of these values is provided in Table 1. Figure 2b displays mass-weighted terminal velocity for each run for a range of graupel mixing ratios, using these new values for  $a_g$ .

Previous studies have evaluated the difference in hail and graupel simulations by using a double-moment graupel distribution and modifying the fall speed parameters of that class (Bryan and Morrison 2012; van Weverberg et al. 2011, 2012b; Morrison and Milbrandt 2011). In this study, a microphysics scheme with a single-moment graupel class with a fixed distribution intercept  $N_0$  was purposefully chosen to allow direct manipulation of the size distribution through that value,

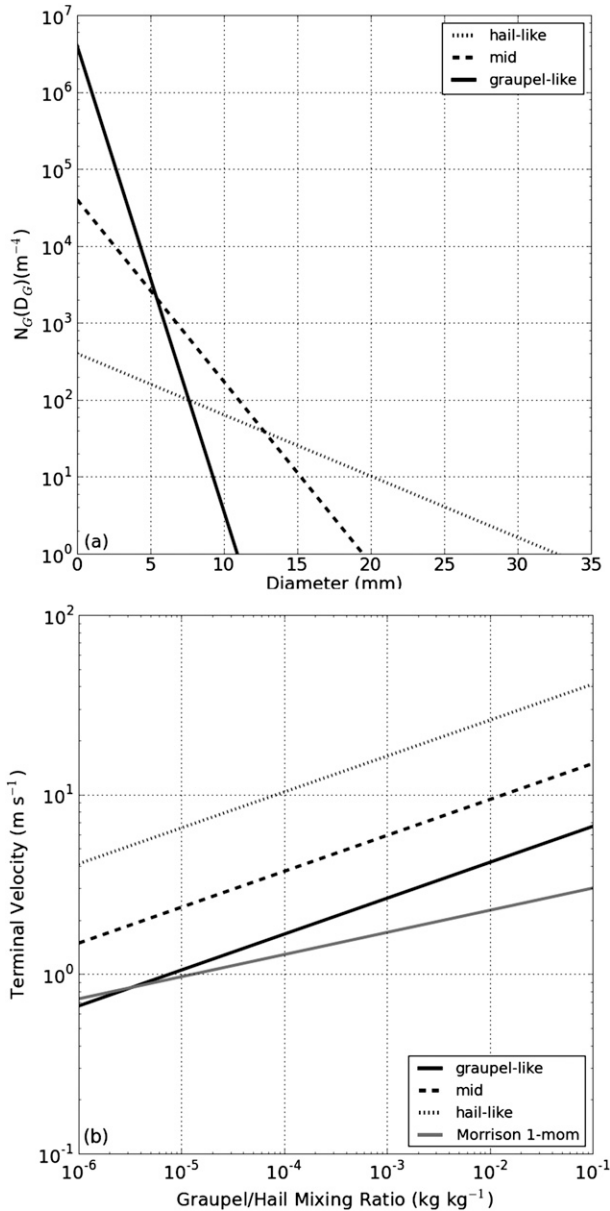


FIG. 2. (a) Graupel hydrometeor size distributions for the model runs given in Table 1. This assumes a graupel mixing ratio of  $1 \text{ g kg}^{-1}$  and air density of  $1 \text{ kg m}^{-3}$ . (b) Mass-weighted mean graupel hydrometeor terminal velocity ( $\text{m s}^{-1}$ ) for a range of graupel mixing ratios ( $\text{kg kg}^{-1}$ ) as a function of four different schemes. Temperature is fixed at 268.15 K, and pressure at 900 hPa. The fast graupel fall speed is equivalent to that of the hail-like system. The Morrison fall speed uses the single-moment Morrison scheme described in Bryan and Morrison (2012).

as it is hypothesized that both mean hydrometeor size and fall speed should have an effect. Within Bryan and Morrison (2012), the differences between the faster- and slower-falling graupel simulations were evident in both the one- and two-moment tests, suggesting comparison

among this studies' single-moment sensitivity tests should still be instructive.

It is evident from Fig. 2a and (2) that a decrease in the hydrometeor intercept yields an overall increase in the number of large hydrometeors while decreasing the number of small hydrometeors, all else being equal. This change in mean hydrometeor size will increase the mean terminal velocity of the distribution. This will result in less residence time in the downdraft and increased downward precipitation flux (Gilmore et al. 2004a), but also less time for melting and evaporation. Larger hydrometeors have less surface area-to-volume ratio, which can also reduce the melting and evaporation rates (van den Heever and Cotton 2004). To examine the relative contributions of reduced mean size and reduced fall speed, another sensitivity test was designed that contains a large graupel intercept parameter and small mean size, but with fast fall speeds. This test is termed "fast graupel," and its specific parameters are also given in Table 1.

Separate tests were conducted varying the graupel density in isolation, but little effect was found on the bowing and convective development within the simulations, similar to the results noted in Bryan and Morrison (2012).

In the second experiment, a comparison of the 5- and 6-class schemes is used to examine the importance of graupel as a class in simulating this type of convective system. These will be termed the "graupel" and "no graupel" simulations, and were run using the WSM5 and WSM6 schemes.

### 3. Results from hail–graupel comparison

Deep convection initiated almost immediately in all five simulations as the cold dam began propagating eastward. By 2 h into these simulations, a mesoscale convective system structure with convective line and minimal stratiform precipitation region had appeared (not shown). By 0235 (2 h, 35 min), the stratiform precipitation predominately trailed the convective line in all simulations.

The convective line in each simulation began to bow at 0240, 0250, 0300, and 0220 simulation time in the graupel-like, mid, hail-like, and fast graupel simulations, respectively. All four systems as they started to bow are shown in Fig. 3. Figure 3 also is representative of the differences in these systems throughout each simulation. The graupel-like system was more extensive, with high reflectivities even in the stratiform region. The convective line was over 20 km wider than that of the hail-like system, similar to Bryan and Morrison (2012), and contained peak reflectivities approximately 5 dBZ higher.

TABLE 1. Names of model simulations with the intercept value ( $n_{0G}$ ), density ( $\rho_G$ ), and fall speed parameters ( $a_G$ ,  $b_G$ ) used in the hail/graupel comparison experiment, and graupel removal experiment. The default values in WSM6 are those of the “graupel” simulation.

Simulation name	Microphysics scheme	Intercept ( $n_{0G}$ ; $m^{-4}$ )	Density ( $\rho_G$ ; $kg\ m^{-3}$ )	Fall speed coef ( $a_g$ )	Fall speed coef ( $b_g$ )
First expt: Hail/graupel comparison					
Hail-like	WSM6	$4 \times 10^2$	900	330	0.8
Mid	WSM6	$4 \times 10^4$	700	285	0.8
Graupel-like	WSM6	$4 \times 10^6$	300	270	0.8
Fast graupel	WSM6	$4 \times 10^6$	300	1700	0.8
Second expt: Removal of graupel class					
No graupel	WSM5	—	—	—	—
Graupel	WSM6	$4 \times 10^6$	500	330	0.8

There was also no clear “transition zone” or region of lesser reflectivity between the convective line and the more intense stratiform region (Fig. 3a), which is unrealistic compared to typical observed squall lines (Biggerstaff and Houze 1991, 1993), but generally expected with single-moment microphysics schemes (Bryan and Morrison 2012). The mid system contained stratiform precipitation over about the same area, but of much weaker intensity (Fig. 3b). The stratiform regions of the hail-like and fast graupel systems covered the smallest area and were less intense (Figs. 3c,d), although the fast graupel convective line was most intense of any simulation (Fig. 3d).

The fast graupel system began bowing first, followed by the graupel-like, mid, and hail-like systems at 0220,

0240, 0250 and 0300, respectively. Reasons for this distinction will be discussed in the following paragraphs. Significant differences were also observed in the mean system speed, determined by cold pool position: the fast graupel ( $23.1\ m\ s^{-1}$ ), graupel-like ( $21.4\ m\ s^{-1}$ ), and mid ( $18.7\ m\ s^{-1}$ ) systems were all faster than the hail-like system ( $16.7\ m\ s^{-1}$ ). All of the systems continued bowing through the end of the run time (not shown).

#### a. System-relative rear-to-front flow

As this work is primarily interested in the behavior of the system while bowing, vertical cross sections will be examined through the region of the storm that later exhibits bowing development. Similar behavior can be seen throughout the segment of the line that bows.

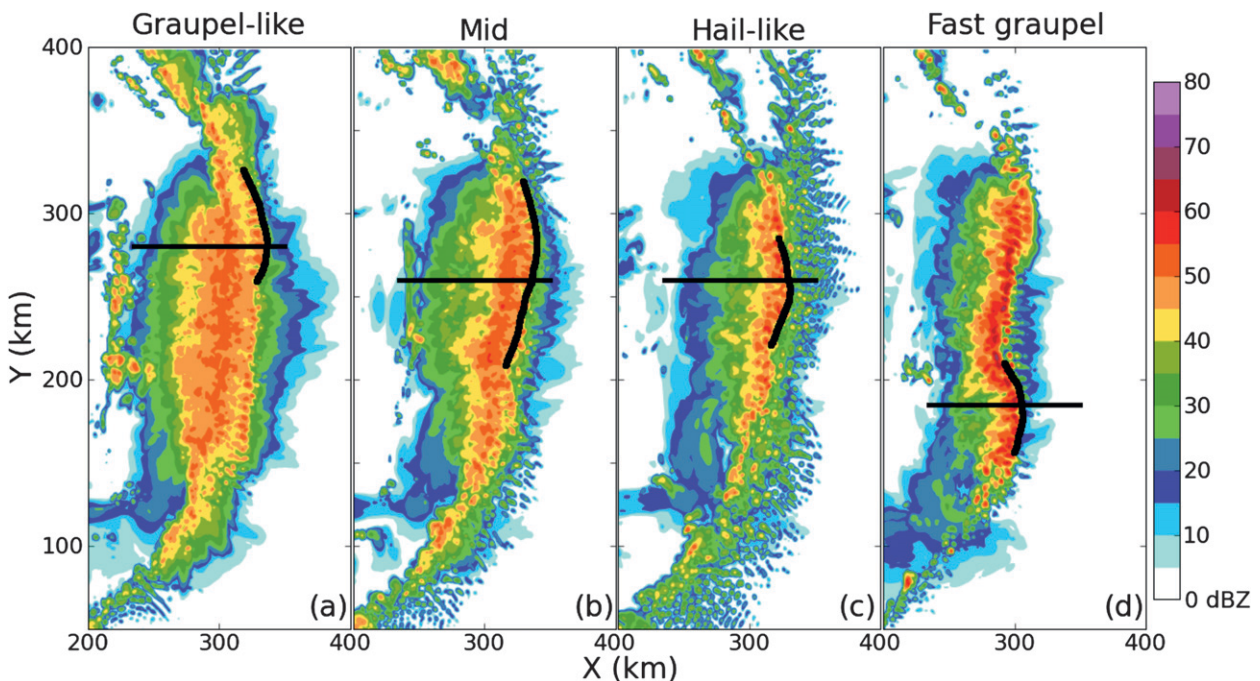


FIG. 3. Simulated composite reflectivity for the (a) graupel-like, (b) mid, (c) hail-like, and (d) fast graupel systems as they each begin to bow, at the 0240, 0250, 0300, and 0220 simulation time, respectively. Thick black lines delineate bowing segments. Thin black lines show location of later vertical cross-sectional figures. Simulated composite reflectivity calculated as in Stoelinga (2005), but modified to use the WSM6 scheme’s temperature-dependent snow intercept parameter.

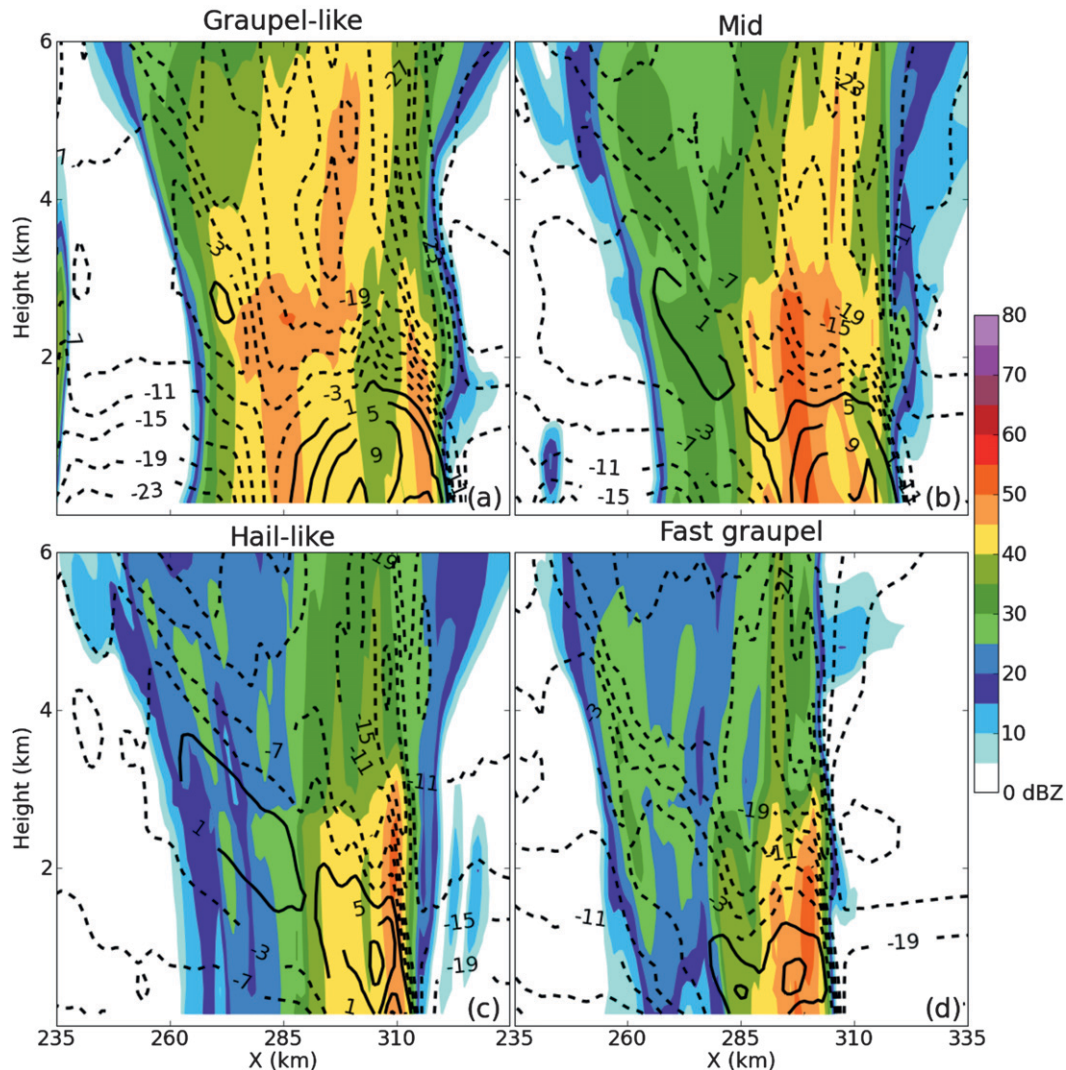


FIG. 4. The 0–6-km vertical cross sections of the (a) graupel-like, (b) mid, (c) hail-like, and (d) fast graupel systems, at the time each developed significant system-relative rear-to-front flow: 0230, 0235, 0245, and 0220 simulation time, respectively. These cross sections are taken along the black line shown in Fig. 3; plotted values are averages 5 km either side of the cross section. Simulated reflectivity (color) and storm-relative line-normal winds in the plane of the cross section (black contours,  $4 \text{ m s}^{-1}$ , negative dashed) are shown.

Along-line averaging was performed 5 km on either side of the chosen cross section (shown in Fig. 3). Rear-to-front system-relative flow first appeared in the fast graupel system at 0130, the graupel-like system at 0140, then mid at 0145, and finally the hail-like system at 0215 (not shown). The midlevel (3–6 km) low pressure region formed in each system in the same order. The fast graupel (hail-like) system's low pressure region was most (least) intense; causes of this different pressure perturbation strength will be discussed in more detail in the next section.

Immediately after its formation, the rear-to-front flow in each case was located only immediately rearward of

the updraft, and at the lowest levels in the simulation. As each run progressed the rear-to-front flow extended farther to the rear of the storm, similar to the gravity wave-generated rear-to-front flow in Pandya and Durran (1996) and Pandya et al. (2000). Shortly before each system bowed, this flow became more evident (Fig. 4). In the graupel-like system, this rear-to-front flow was spread along the surface within the stratiform region; little ambient airflow into the rear of the system occurred nor descent from aloft (Fig. 4a). The same was true of the flow in the fast graupel system, although the rear-to-front flow was weaker, and concentrated closer behind the convective line.

In the mid system, the rear-to-front flow began aloft in the rear of the stratiform region just below the melting level, and descended to the surface fairly quickly approximately 25 km behind the convective updraft (Fig. 4b). The rear-to-front flow in the hail-like system began in the same place as the mid system, but remained aloft until immediately before the convective updraft, and then descended to the surface (Fig. 4a). These simulations agree with results noted by Lafore and Moncrieff (1989), Weisman (1992), and Pandya and Durran (1996) that rear-to-front flow in systems with extensive stratiform precipitation and microphysical cooling remains closer to the surface much farther rearward of the convective line.

The peak rear-to-front flows in this study were even shallower than those observed by Lafore and Moncrieff (below 1 km as opposed to approximately 3 km; see their Fig. 11b). A significantly different microphysics scheme was used in the Lafore and Moncrieff simulations. Highly altered evaporation and melting rates, and therefore dissimilar low-level stratiform vertical motion and resultant depth of rear-to-front flow, are possible. The lack of surface friction and boundary layer parameterization in this simulation could also have had an effect. In any case, rear-to-front flow, which extends to the surface farther behind the convective line, at least temporarily, appears to be associated with new bowing development as it aids the necessary updraft tilt of the convective line (Weisman 1993; Weisman and Rotunno 2005; James et al. 2006). While systems with surface-based rear-to-front flow are expected to dissipate more quickly than systems with elevated rear inflow, that does not preclude them from initiating bowing development more quickly as well (Weisman 1992; Weisman 1993; James et al. 2006).

### b. Midlevel pressure and buoyancy perturbations

The midlevel pressure perturbation can be related to the buoyancy gradient with respect to height through

$$\frac{1}{\rho_0} \nabla^2 p' = -\nabla \cdot (\mathbf{v} \cdot \nabla \mathbf{v}) + \frac{\partial B}{\partial z}, \quad (4)$$

where  $p'$  is the perturbation pressure,  $\mathbf{v}$  is the horizontal wind vector, and  $B$  is buoyancy. Buoyancy is given by

$$B = g \left[ \frac{\theta - \bar{\theta}}{\bar{\theta}} + 0.61(q_v - \bar{q}_v) - q_t \right], \quad (5)$$

where  $g$  is gravitational acceleration,  $\theta$  is potential temperature,  $q_v$  is water vapor mixing ratio,  $q_t$  is the total hydrometeor mixing ratio, and the bars designate environmental conditions. The midlevel buoyancy gradient

is typically positive, due to the warmer updraft overlying the cold pool. Thus, a system with an intense and deep cold pool would also have a strong vertical buoyancy gradient and lower pressure at midlevels.

Cross sections of hydrometeor mixing ratios (Fig. 5), cooling rates (Fig. 6), and vertical motion and pressure perturbation (Fig. 7) are shown from all four simulations at the time of new bowing development in each. Vertically integrated changes in temperature due to melting and evaporation, both minimum and domain-averaged values, are given in Table 2. The graupel-like system contained smaller graupel hydrometeors that were advected rearward, which formed the extensive convective line and stratiform precipitation regions evident in Fig. 5a. The cold pool associated with the graupel-like system was widest (Fig. 5a), and significantly more intense than the hail-like cold pool, as measured by cold pool intensity  $C$  (Fig. 8a);  $C$  is calculated as in Bryan and Morrison (2012),  $C^2 = \int_0^h B dz$ , where  $B$  is given by (5) and  $h$  is the height at which  $B$  becomes 0.

The slower-falling, small graupel hydrometeors resulted in high melting and evaporation rates (Fig. 6a; Table 2) almost 40 km behind the convective line. The deepest portion of the cold pool was actually in the stratiform region, collocated with the largest melting and evaporation rates. Because of this strong and deep cold pool, this system contained large midlevel buoyancy and pressure perturbations (Fig. 7a). Note that the pressure perturbations are relative, calculated with respect to the domain mean pressure field at the time, so perturbations only need to be lesser than their surroundings to be considered “low,” not absolutely negative.

The hail in the hail-like system fell almost immediately out of the updraft because of its much larger size (Fig. 5c), and was able to reach the surface before much melting occurred. Small amounts of cooling by melting and evaporation are evident in Fig. 6c, and associated cooling rates are small (Table 2). The peak magnitudes of cooling were located less than 10 km rearward of the system updraft. Cloud ice content was also much higher in the upper levels of the storm, consistent with other studies noting transfer of mass to smaller frozen hydrometeor classes in simulations with hail (Morrison and Milbrandt 2011). The cold pool associated with this system at this time was of weaker intensity (Fig. 8a) and lesser depth. This would correspond well with the slower system noted earlier, as well as weaker midlevel buoyancy and pressure gradients (Fig. 7c).

The fast graupel system produced the most intense cold pool (Fig. 8a), but it was very narrow. (Initial cold pool intensity values for all simulations were  $18.4 \text{ m s}^{-1}$ .) Little condensate remained aloft as its

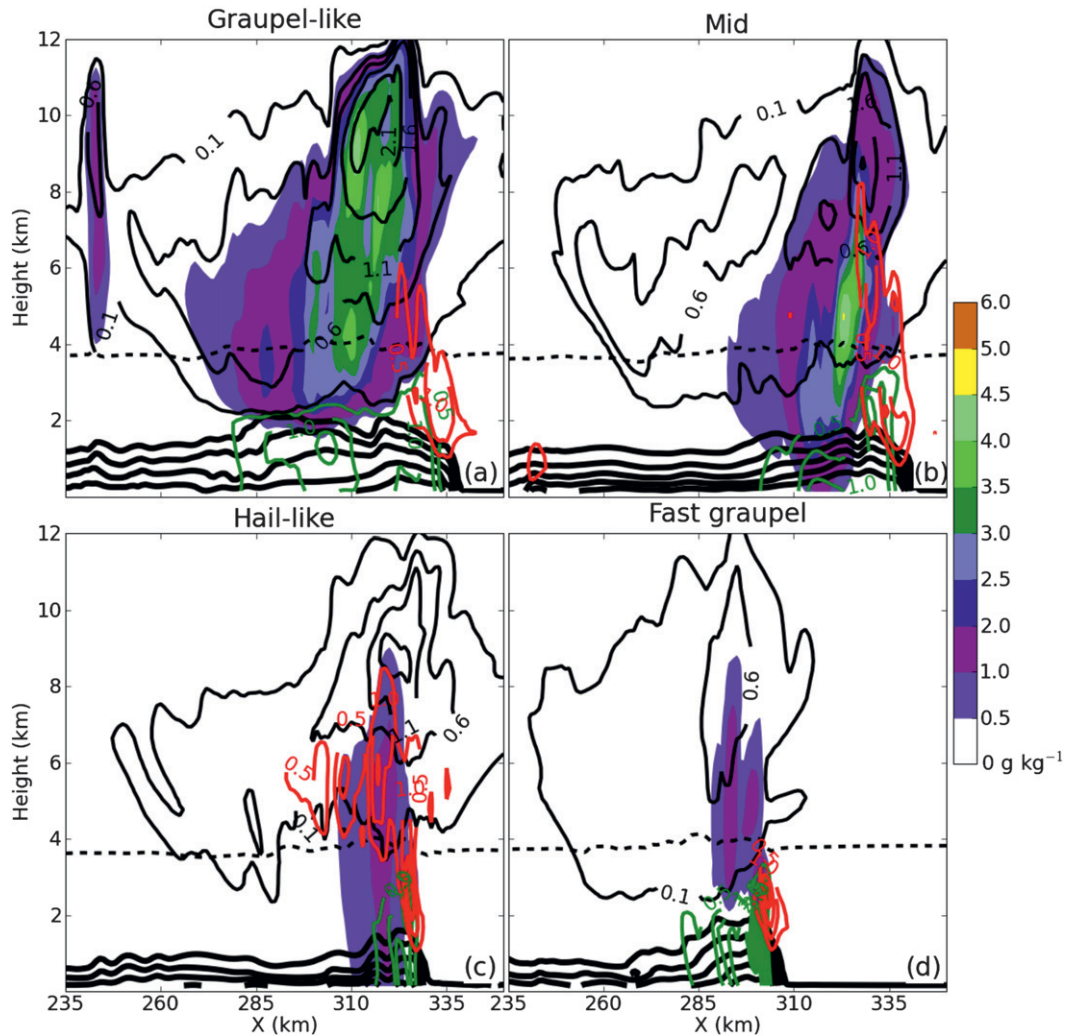


FIG. 5. Mixing ratios ( $\text{g kg}^{-1}$ ) of graupel (filled contours), cloud water and ice (red,  $0.5 \text{ g kg}^{-1}$ ), rainwater (green,  $0.5 \text{ g kg}^{-1}$ ), and snow (thin black,  $0.5 \text{ g kg}^{-1}$ , starting at  $0.1 \text{ g kg}^{-1}$ ); the thick solid black lines are cold pool potential temperature perturbation contours every 2 K. Thin dashed black line is the melting level. (a)–(d) Vertical cross sections as in Fig. 4, but from 0 to 12 km, and as each simulation begin to bow, at 0240, 0250, 0300, and 0220 simulation time.

graupel hydrometeors fell quickly out of the updraft once formed (Fig. 5d). Because the mean size of these hydrometeors was quite small, the increased surface area-to-volume ratio still allowed a significant amount of melting and subsequent evaporation to occur (Fig. 6d), but it was concentrated in an area immediately behind the convective line. This is evident in Table 2 as the peak magnitude of cooling by melting of the fast graupel system is the lowest of all the simulations, but the domain mean less so. The midlevel pressure gradient was most intense compared to the other systems' (Fig. 7d). This indicates the mean size of the graupel hydrometeor is important as well as its fall speed when determining cooling rates.

### c. Microphysical effects on bowing

Prior to bowing, the convective updrafts of all four simulations were similar in intensity (Fig. 8c) and minimally tilted. The updrafts in the graupel-like system were slightly stronger, due largely to increased freezing rates (not shown, likely from increased concentrations of smaller hydrometeors). The updrafts in the mid and hail-like systems were slightly weaker, but still minimally tilted.

As bowing occurred, however, each system's convective updrafts became additionally tilted (Fig. 7), as would be expected. The updraft of the fast graupel and graupel-like systems, with their most intense cold pool

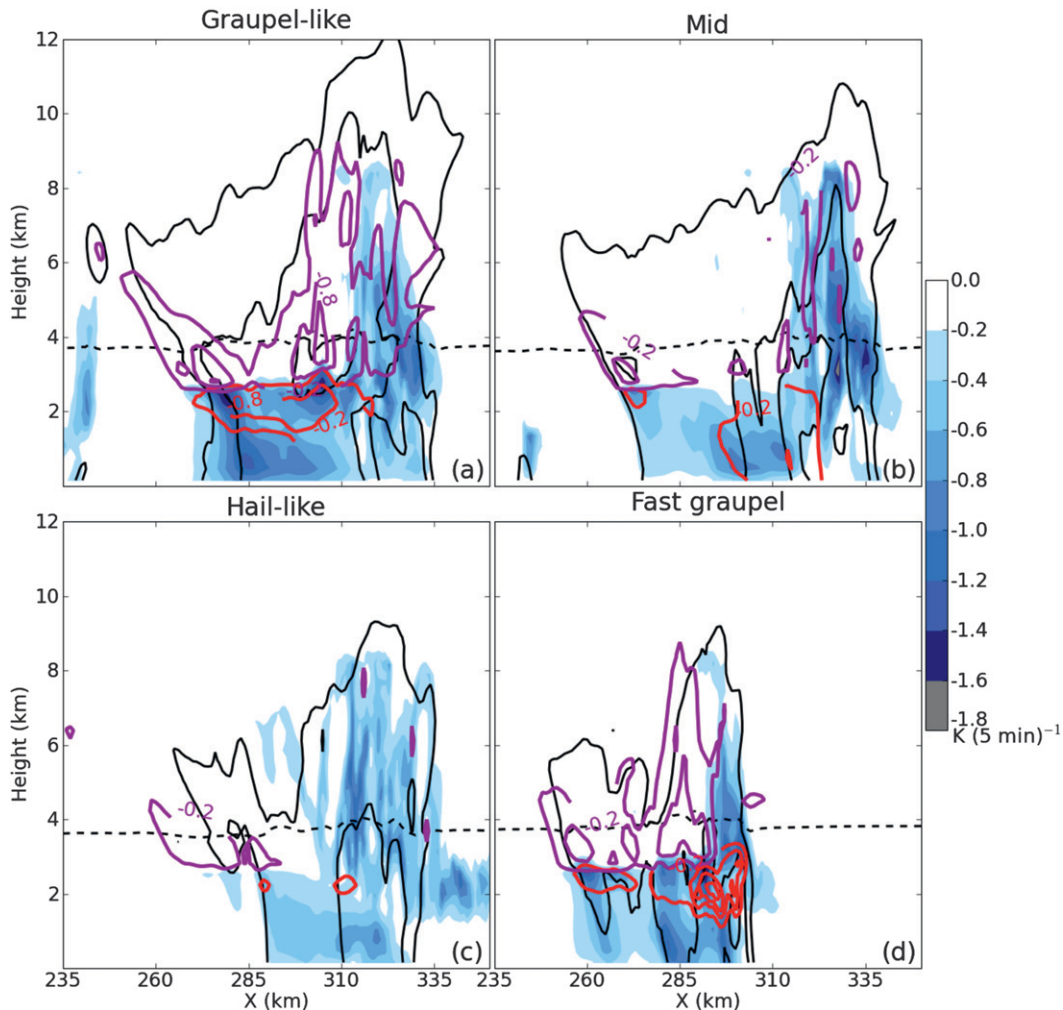


FIG. 6. Cooling rates [ $\text{K} (5 \text{ min})^{-1}$ ] of evaporation (blue shading), melting [red,  $0.6 \text{ K} (5 \text{ min})^{-1}$ , starting at  $-0.2 \text{ K} (5 \text{ min})^{-1}$ ], and sublimation [purple,  $0.6 \text{ K} (5 \text{ min})^{-1}$ , starting at  $-0.2 \text{ K} (5 \text{ min})^{-1}$ ]. Thick solid black lines are the simulated reflectivity at 25, 40, and 50 dBZ. Thin dashed black line is the melting level. Vertical cross sections are as in Fig. 5.

and surface-based rear-to-front flow (Figs. 8a and 4a,d), tilted farther rearward first, and therefore also bowed first. At the time of bowing, the tilt of the convective updraft between 0 and 6 km aloft was approximately 20–25 km in these two systems. The tilt of the graupel-like system was larger than the fast graupel system, possibly because of the larger magnitude of the rear-to-front flow further adding to the negative vorticity associated with the cold pool. However, both tilts were large enough to initiate bowing. The updraft of the hail-like system, with its weaker cold pool and more elevated rear-to-front flow (Figs. 8a and 4c), increased its updraft tilt later and therefore bowed last as well. Also evident was an increase in the maximum downdraft velocity associated with each system immediately prior to bowing (Fig. 8d).

By 0400, just over an hour after all four systems had bowed, the convective updraft in the graupel-like

simulation had appeared to separate into two updrafts, one at lower levels from 0–3 km, and the other at mid- and upper levels, from 3–9 km (not shown). The lower-level updraft was approximately 20 km ahead of the upper-level one. The convective updrafts in the mid and hail-like systems were each somewhat less tilted: the mid system over approximately 15 km, and the hail-like system over about 10 km. By 0515, because of the extreme updraft tilt, the updraft associated with graupel-like system was slightly weaker than the mid system, and weaker yet than the most upright hail-like system (Fig. 8c). The cold pools associated with each were growing correspondingly weaker as well (Fig. 8a). Surprisingly, the fast graupel system updraft strength remained similar to the less tilted hail-like updraft throughout; possibly the result of a more narrow cold pool and slower rear-to-front flow (not shown).

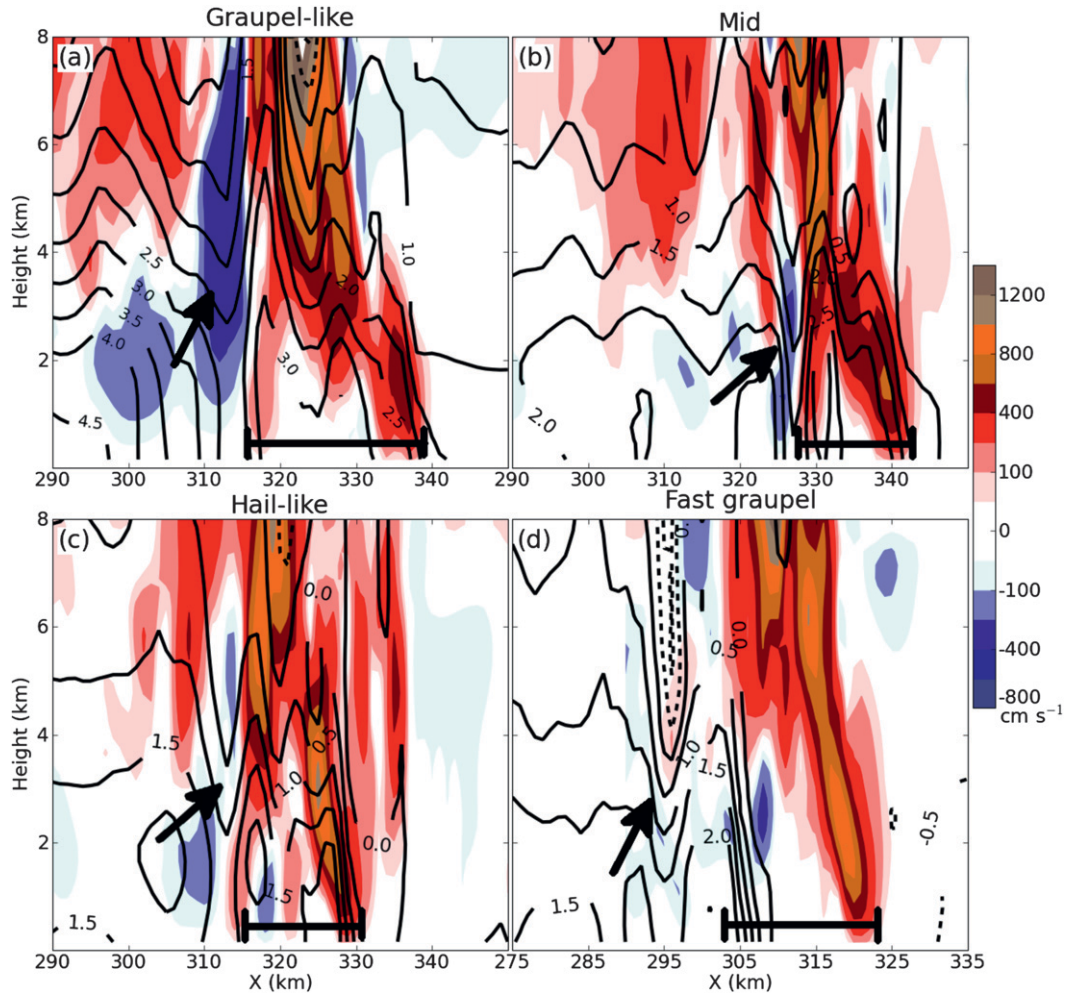


FIG. 7. Vertical motion (color shading,  $\text{cm s}^{-1}$ ) and relative perturbation pressure (black, 0.5 hPa, negative dashed), at the same times as in Fig. 5. Perturbation pressure was calculated by subtracting the mean total domain pressure profile from the total pressure field. These cross sections are a 60-km subset of the cross sections shown in Fig. 5. The black arrows in each figure point to the low pressure perturbation discussed in the text. The brackets show the total tilt of the convective updraft over heights from 0 to 6 km.

The increased evaporation rates of the graupel-like system resulted in its domain-maximum precipitation rates being smallest; because so much of the hail in the hail-like system reached the surface without even melting, its maximum precipitation rates were the highest (Fig. 8b). Additionally, many of the graupel-like system’s frozen hydrometeors were still aloft throughout the simulation due to their slower fall speeds. In the fast graupel simulation these hydrometeors were able to reach the surface, producing large maximum precipitation rates. Peak precipitation rate was more sensitive to hydrometeor fall speed than mean size. Total precipitation accumulation was as well; the mean total gridpoint accumulation of liquid and frozen precipitation in the fast graupel and graupel-like simulations

(7.88 and 7.90 mm) were less than the mid mean total (8.39 mm) and significantly less than the hail-like mean total (10.83 mm).

*d. Comparison to other studies*

Because the WSM6 scheme is also single-moment with respect to raindrops, increased evaporation was expected in the stratiform rain region as the fixed hydrometeor intercept would keep the concentration of rain drops artificially high compared to the varying concentrations in a double-moment scheme, as discussed in Bryan and Morrison (2012). However, the extreme evaporation rates seen in that study’s single-moment Morrison simulation, to the point of the stratiform precipitation region not reaching the surface, were

TABLE 2. Minimum and domain-averaged vertically integrated change in temperature due to melting and evaporation [ $\text{K} (5 \text{ min})^{-1}$ ] at the time of bowing in each simulation. Integration was over the entire domain depth.

Simulation name	Melting		Evaporation	
	Min	Domain mean	Min	Domain mean
First expt: Hail/graupel comparison				
Hail-like	-0.068	$-8.78 \times 10^{-4}$	-0.869	$-1.49 \times 10^{-2}$
Mid	-0.199	$-2.42 \times 10^{-3}$	-1.009	$-1.83 \times 10^{-2}$
Graupel-like	-0.361	$-3.15 \times 10^{-3}$	-0.736	$-2.10 \times 10^{-2}$
Fast graupel	-0.795	$-2.41 \times 10^{-3}$	-0.771	$-1.34 \times 10^{-2}$
Second expt: Removal of graupel class				
No graupel	-0.154	$-1.63 \times 10^{-3}$	-1.026	$-1.70 \times 10^{-2}$
Graupel	-0.368	$-3.63 \times 10^{-3}$	-0.956	$-2.38 \times 10^{-2}$

not seen in any of these simulations. The graupel fall speed parameters in the Morrison scheme, at the mixing ratio values typically seen in the stratiform region (on the order of  $1 \text{ g kg}^{-1}$ ), result in slightly slower fall speeds (Fig. 2b). These slower fall speeds would allow increased melting and evaporation rates. Additionally, the fixed rain intercept parameter in the WSM5/6 schemes is  $8 \times 10^6$ , slightly lower than the  $10^7$  value specified in the single-moment Morrison scheme used in that study, meaning the overestimation of concentration in the stratiform region should not be quite as severe. These factors combined could have lessened the evaporation rates in this study.

The result of the graupel-like system creating a more intense cold pool than the hail-like system is in contrast to Gilmore et al. (2004a), van Weverberg et al. (2011, 2012b), and Morrison and Milbradt (2011), which found the hail system created more intense cold pools. In general, in those studies the fast hail fall speeds increased the downward precipitation flux, which increased the melting and evaporation rates. The graupel hydrometeors with their relatively slow fall speeds remained aloft in those systems. Large amounts of graupel were certainly falling below the melting level in this graupel-like simulation (Fig. 5a). Additionally, many of the hail-like hydrometeors were still frozen upon reaching the surface (Fig. 5c), unlike in those other studies, reducing the opportunity for latent cooling.

One possible reason for this difference lies in the initial environment. The environmental soundings used in the simulations of Gilmore et al. (2004a), van Weverberg et al. (2011), and Morrison and Milbradt (2011) had lower CAPE values compared to this study; 2200, 1000, and  $2200 \text{ J kg}^{-1}$ , respectively, compared to an initial CAPE of  $3752 \text{ J kg}^{-1}$ . Those same studies also had significantly higher deep-layer shear values, as all three studies were simulating supercells: 0–5-km shear of 30 and  $50 \text{ m s}^{-1}$ , 0–6-km shear of  $28 \text{ m s}^{-1}$ , and 0–7-km

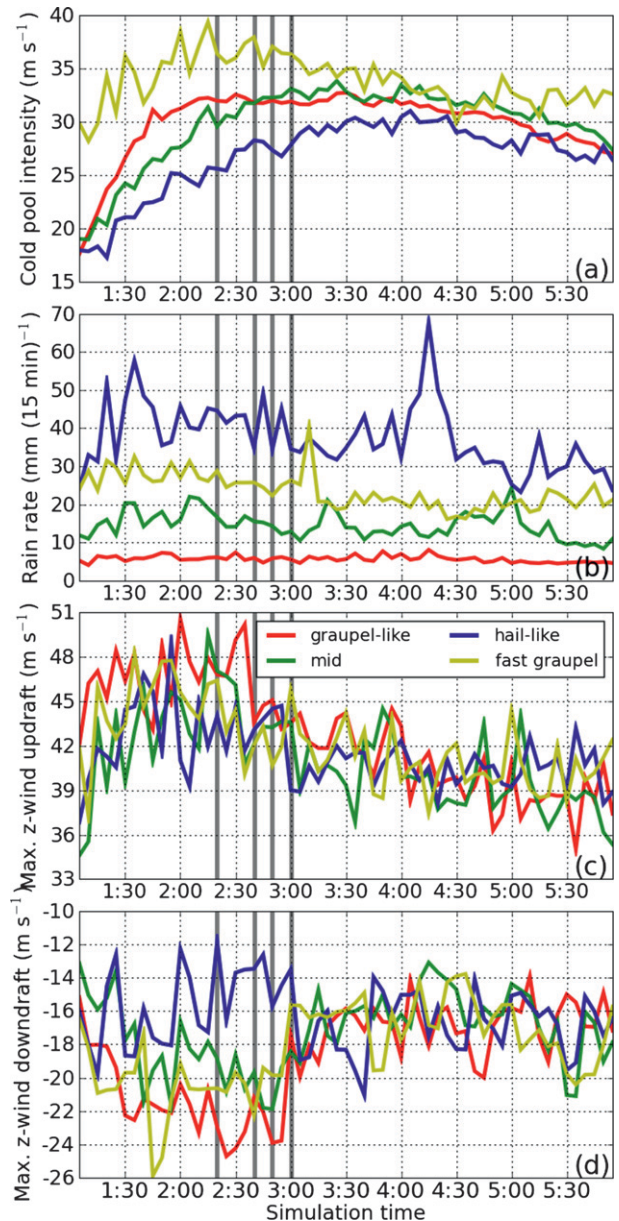


FIG. 8. Comparison of graupel-like (red), mid (green), hail-like (blue), and fast graupel (yellow) simulations from 1- to 6-h simulation time. (a) Maximum  $C$  ( $\text{m s}^{-1}$ ), (b) maximum rain rate [ $\text{mm} (15 \text{ min})^{-1}$ ], (c) maximum  $z$ -wind updraft ( $\text{m s}^{-1}$ ), and (d) maximum  $z$ -wind downdraft ( $\text{m s}^{-1}$ ). Maximum and minimum values are calculated over 5-min intervals over the entire domain. The four thick gray lines are the times new bowing development initiates in the fast graupel, graupel-like, mid, and hail-like simulations (0220, 0240, 0250, and 0300, respectively).

shear of  $40 \text{ m s}^{-1}$ , respectively, compared to the 0–5-km shear in this study of  $14.2 \text{ m s}^{-1}$ , almost all of which is in the 0–2.5-km layer. Meanwhile, the colder graupel-like cold pool results of this study agree with van den Heever and Cotton (2004) and Bryan and Morrison (2012), both

of which simulated convection in environments with higher CAPE (3130 and 4200 J kg<sup>-1</sup>) and weaker shear (0–5-km shear of approximately 20 m s<sup>-1</sup>, and 0.5–10-km shear of 10 m s<sup>-1</sup>). Changes in CAPE and shear would affect both updraft strength and storm structure, possibly modifying the time spent aloft by hail/graupel hydrometeors and affecting the resulting microphysical cooling rates. For example, van Weverberg et al. (2012a) found a positive correlation between peak updraft strength and the increase in rain rate due to hail-like graupel modifications.

In the context of bow echoes, an increase in shear would change the cold pool–environmental shear vorticity balance, increasing the amount of cooling required to overwhelm that balance and possibly delaying bowing. Thus, the sensitivities of the microphysical variations described herein to changes in the environment, specifically an increase in 0–5-km shear, should be tested. However, within this environment of weaker low-level shear changing the graupel parameter to take on more hail-like characteristics acted to diminish both the microphysical cooling and warming within the system. This occurred as a result of both the increased mean size and the increased mean fall speed. In turn, the strength and depth of the cold pool and midlevel buoyancy gradient was decreased, and weakened the midlevel pressure perturbation. The rear-to-front flow associated with the system was not as fast, and did not descend to the surface until almost reaching the convective line. Hence, the convective updraft was slower to tilt upshear and bowing did not develop as quickly.

#### 4. Results from removal of graupel class

The WSM5 and WSM6 schemes are identical except for the inclusion of graupel as a class in the 6-class scheme (Lim and Hong 2010). Simulations using both the 5- and 6-class schemes (no-graupel and graupel simulations, see Table 1) were run to examine the importance of graupel as a class. These comparisons will continue to explore the effect of changes in microphysical cooling rates on bowing initiation, as well as the effect slowly falling frozen hydrometeors have on cold pool strength.

The no-graupel simulation quickly developed a large stratiform shield ahead of the convective line as early as 0110 (not shown) due to large concentrations of small and slowly falling snow being advected ahead of the updraft; the convective line itself was intense but narrow compared to the graupel simulation. The graupel simulation did not develop a trailing stratiform shield until approximately 0200 (not shown), but the convective line was thick and intense. The graupel system also

propagated at a significantly faster speed than the no-graupel system; a discussion of the reason for this will follow.

At 0235, a small segment on the north end of the graupel system began to bow (Fig. 9a), which had developed a small but intense stratiform region. The no-graupel simulation at this time had not bowed, and still contained an extensive amount of leading stratiform precipitation (Fig. 9d). At 0310, the no-graupel simulation's stratiform region had increased in size, and a small segment on its northern end began to bow (Fig. 9e). The graupel simulation continued to bow (Fig. 9b). Neither system dissipated before simulation end (Figs. 9c,f).

Figures 10, 11, and 12 show hydrometeor profile, microphysical cooling rate, and storm-relative line-normal wind cross sections from these two simulations; Table 2 again contains the melting and evaporation cooling rates. Panels a and b in each are from 0235, when the graupel system began bowing. The large leading stratiform shield of snow in the no-graupel simulation is evident in Fig. 10b. The main rain shaft was only about 40 km wide and located almost immediately behind the convective updraft; hence, melting and evaporation rates were concentrated in the same location (Fig. 11b), and the cold pool was narrow (Fig. 10b). It was also less intense than the graupel system's cold pool (Fig. 14a); this was because much of the snow still remained aloft. Meanwhile, the larger, somewhat less easily advected graupel hydrometeors formed a 55-km-wide trailing stratiform region in the graupel system (Fig. 10a).

At this point, when the graupel system was just starting to bow, strong, surface-based rear-to-front flow was evident (Fig. 12a). The low-level convective updraft was stronger in the graupel system (Figs. 13a,b), as were the convective downdrafts that had just intensified immediately prior to this new bowing (Figs. 14b,c). There was a strong midlevel low pressure region resulting from the intense cold pool (Fig. 14a), located directly behind the convective line (Fig. 13a). Thus, the stronger, tilted convective updraft and surface-based rear-to-front flow acted in concert to precipitate earlier new bowing development.

In contrast, the no-graupel convective updraft remained more upright, tilted only about 10 km between 0 and 6 km, in comparison to the graupel-like system's 25 km. Because of the slower onset of latent cooling, the no-graupel system had a less intense cold pool (Fig. 14a), slower and still elevated rear-to-front flow (Fig. 12b), and weaker convective downdrafts (Fig. 14c). The convective updrafts were also weaker (Fig. 14b). Hence, the no-graupel system was not bowing at this time. The low pressure region associated with weaker cold pool was less intense (Fig. 13b).

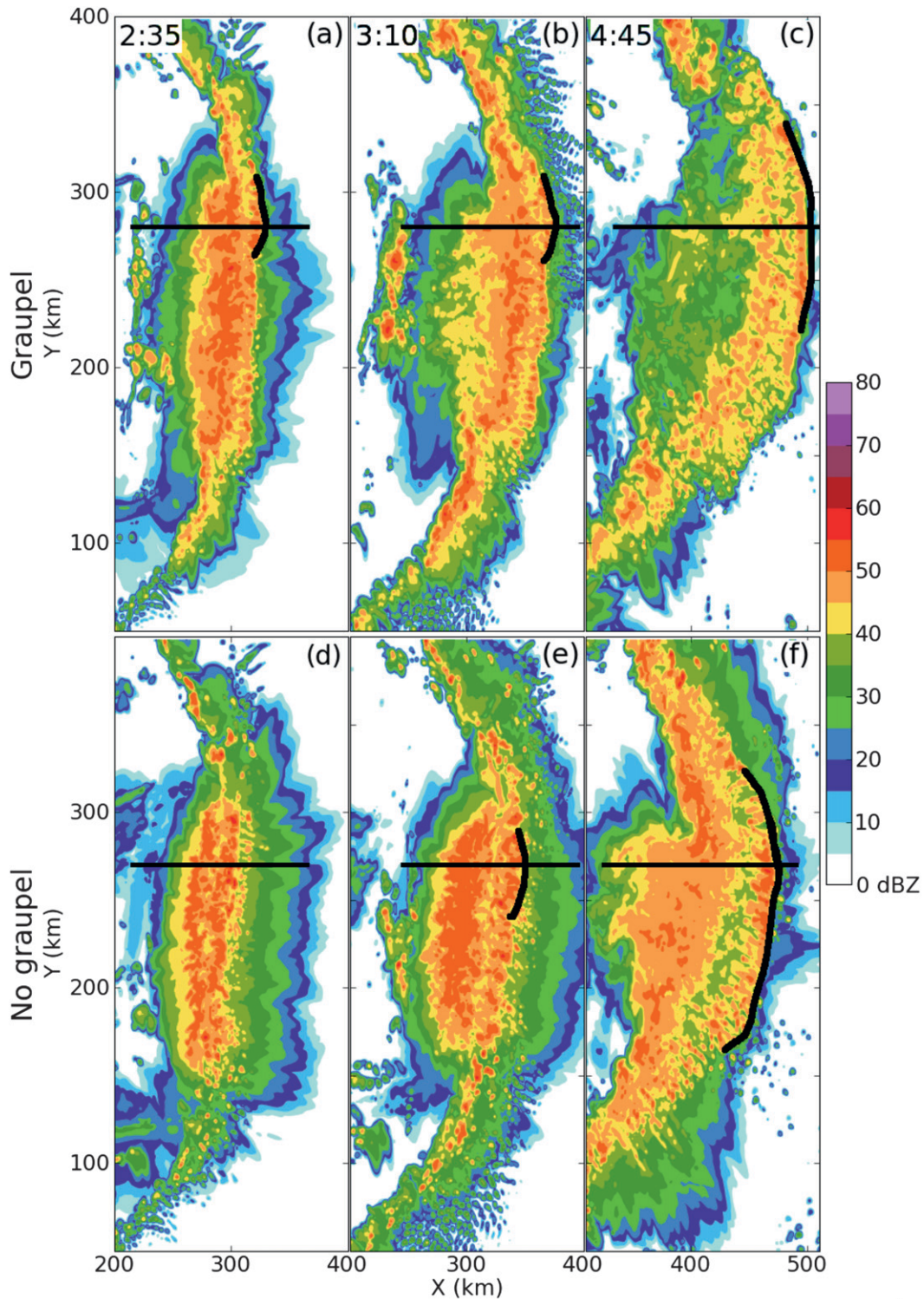


FIG. 9. Simulated composite reflectivity from the (a),(b),(c) graupel and (d),(e),(f) no-graupel simulations. Times at (a),(d) 0235; (b),(e) 0310; and (c),(f) 0445. Simulated reflectivity calculated as in Fig. 3. Thin black lines delineate location of cross sections in subsequent figures. Thick black lines show development of the bowing segment.

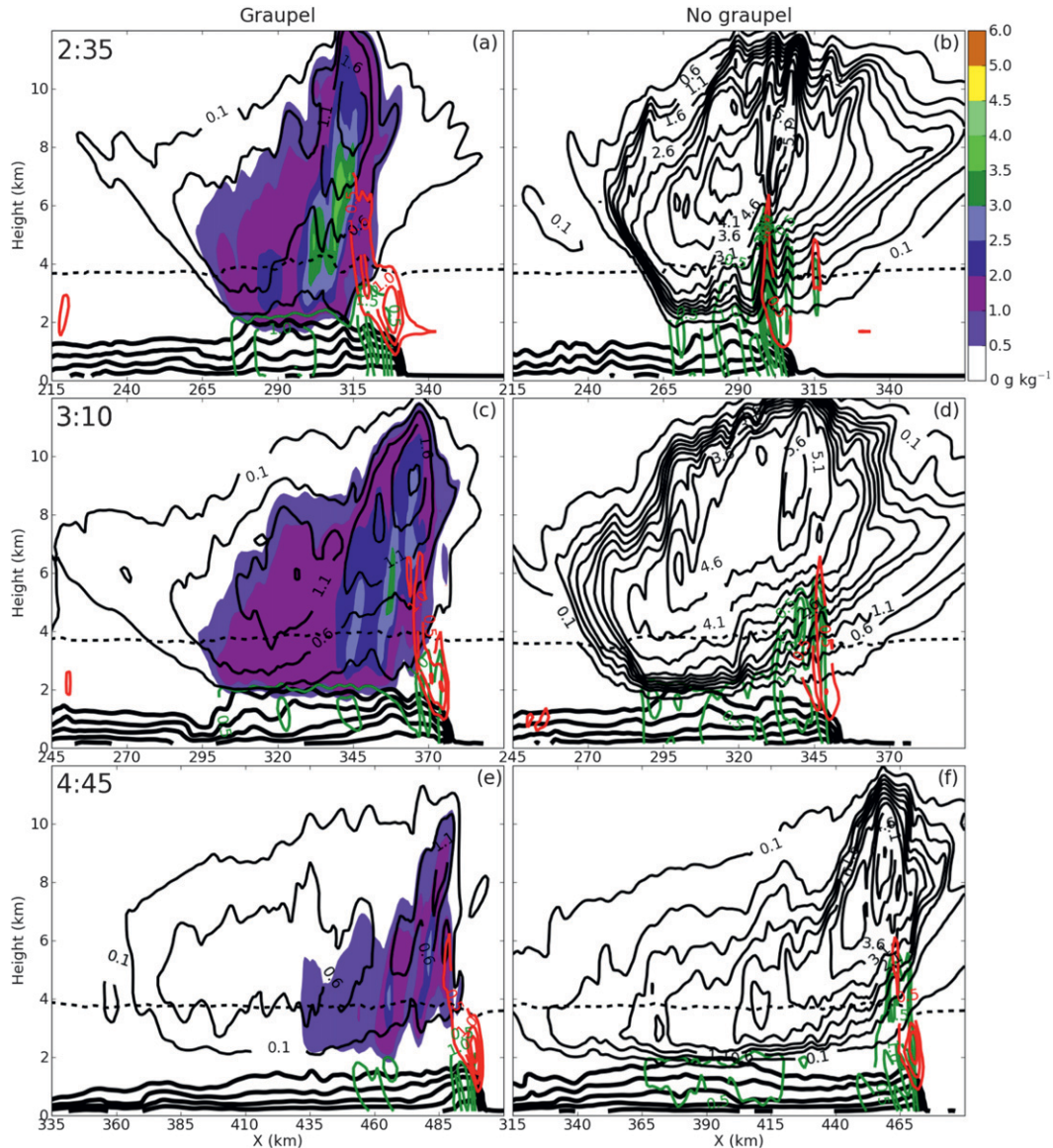


FIG. 10. Mixing ratio cross sections from the (left) graupel and (right) no-graupel simulations at (a),(b) 0235; (c),(d) 0310; and (e),(f) 0445 from cross-sectional lines shown in Fig. 9. Contour values identical to Fig. 5. No color in (b),(d), and (f) as they lack graupel.

The convective updraft of the no-graupel system was weaker than that of the graupel system initially (Fig. 14b), despite being more upright (Figs. 13a,b). This is in contrast to Parker (2010), which found a more tilted updraft should be weaker due to downward acceleration from an increased perturbation pressure gradient. However, freezing rates in the updraft were higher in the graupel system than in the no-graupel system (not shown). This would seem to be counterintuitive, but the graupel hydrometeors fell relatively quickly. The population of supercooled cloud water was located mainly just above the melting level, in both simulations

(Figs. 10a,b). As the graupel hydrometeors fell through this population, cloud water accretion rates were large, increasing the freezing rates. Small liquid drops shed from melting graupel hydrometeors were also advected into the updraft by rear-to-front flow, and further increased the freezing rates upon re-freezing. This “recirculation” process was similar to that examined by Seigel and van den Heever (2013). Meanwhile, significant amounts of the snow in the no-graupel simulation did not fall through the supercooled cloud water until later in the simulation, delaying the addition of freezing by accretion to the overall freezing

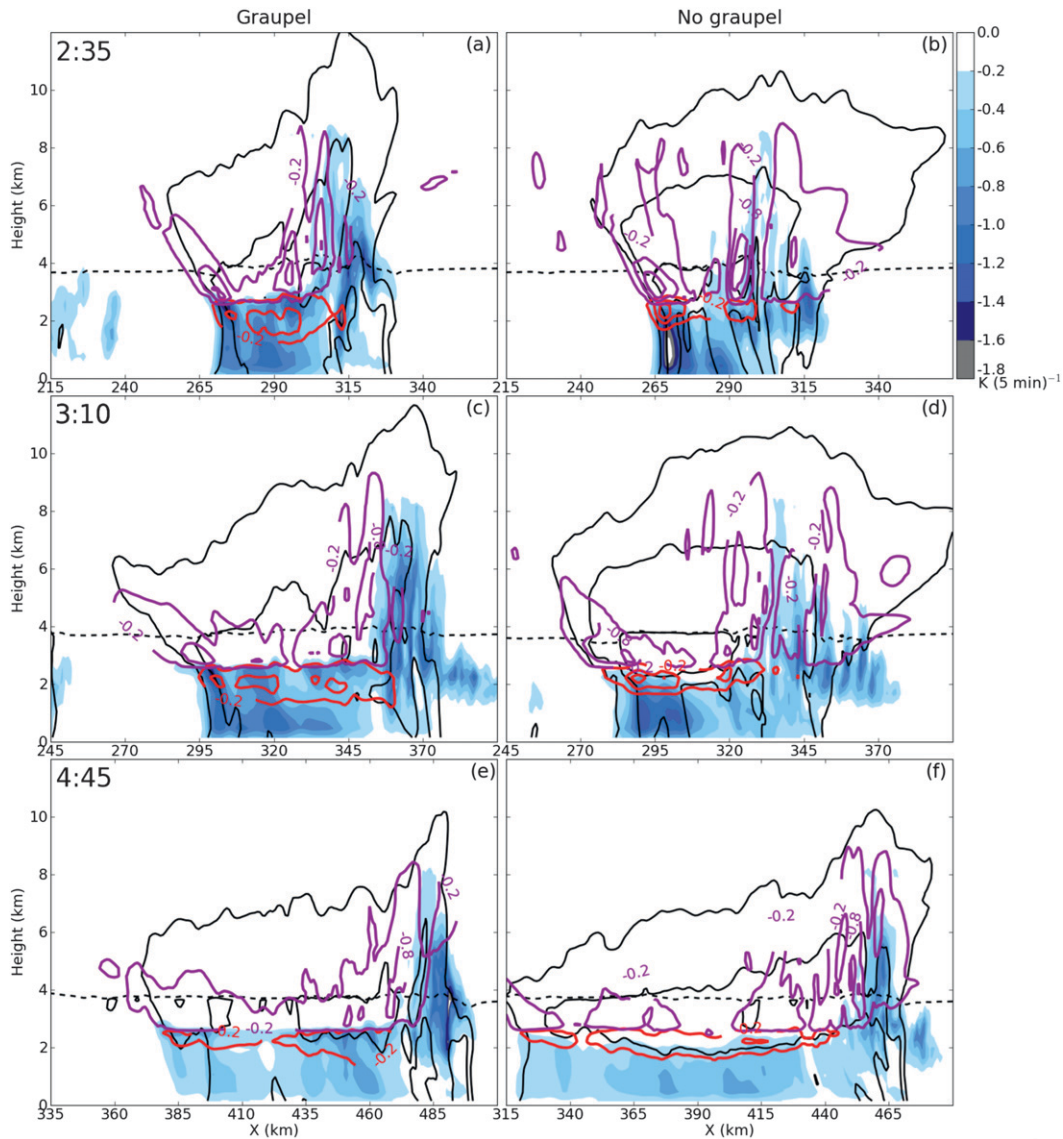


FIG. 11. Microphysical cooling cross sections from the (left) graupel and (right) no-graupel simulations at (a),(b) 0235; (c),(d) 0310; and (e),(f) 0445 from cross-sectional lines shown in Fig. 9. Contour values identical to Fig. 6.

rates. With reduced freezing rates, the no-graupel updrafts were weaker.

At 0310, the no-graupel simulation began to bow. The snow in the stratiform region in the no-graupel simulation had been melting, and then evaporating, over a large region rearward of the convective line for quite some time (Figs. 11d and 10d). The peak evaporation rate was similar to those of the graupel simulation when it began to bow, although the melting rates were not quite as strong (Table 2). The cold pool, while still not quite as large or intense as that of the graupel simulation (Figs. 10c and 14a), was stronger and wider than previously, with a stronger associated midlevel low pressure region (Fig. 13d). The rear-to-front flow had

strengthened and descended to the surface farther behind the convective line (Fig. 12d). The convective updraft was tilted more rearward over the cold pool than previously, approximately 25 km (Fig. 13d), and was about to intensify (Fig. 14b). The convective downdrafts had also strengthened (Fig. 14c). As such, it is not surprising that the no-graupel simulation began to bow.

The graupel hydrometeors falling from the large stratiform region in the graupel system (Fig. 10c) were still producing intense melting and evaporation rates some distance behind the convective line (Fig. 11c); however, these rates were slightly less than those produced by the more numerous, more slowly falling snow

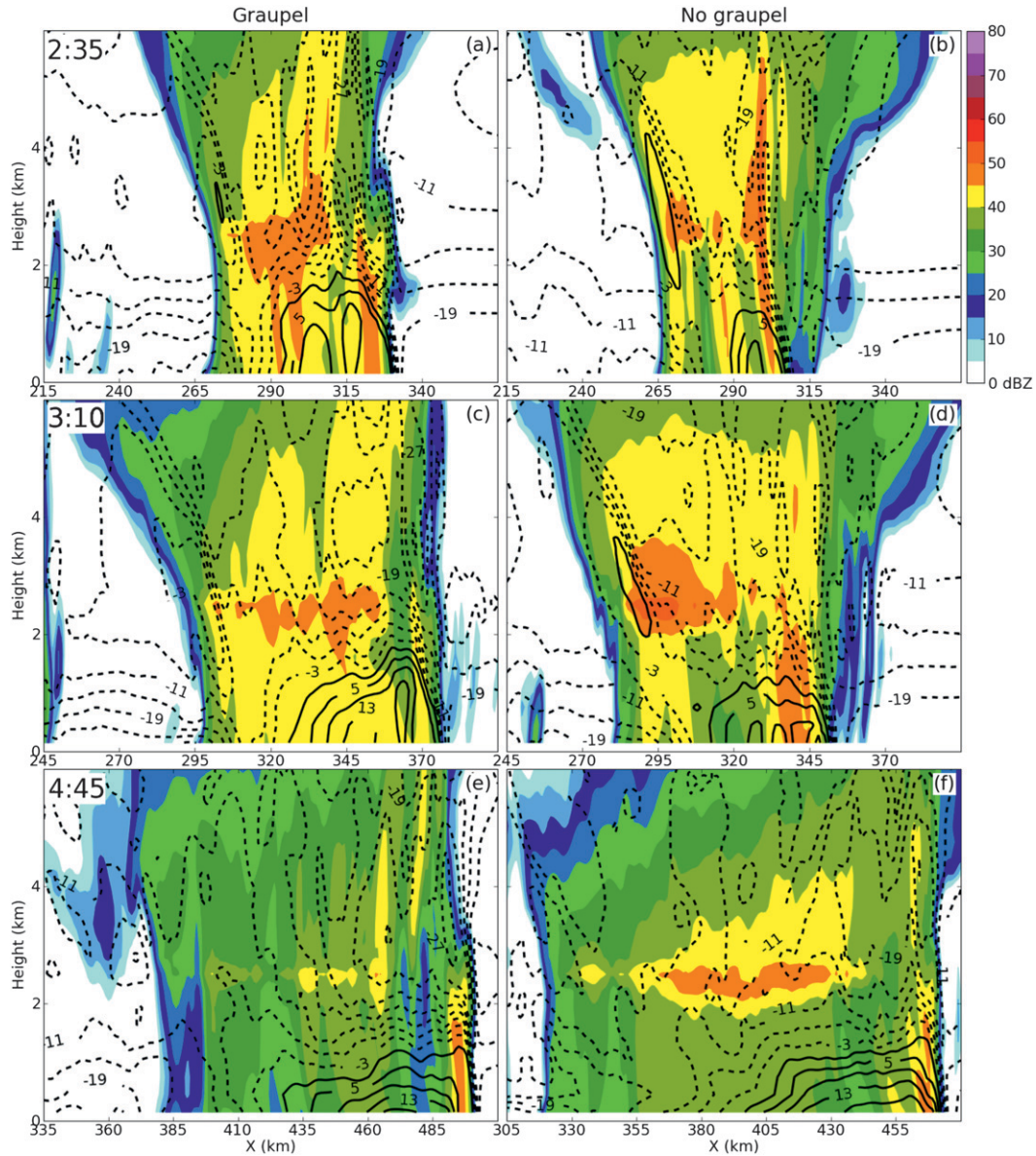


FIG. 12. Storm-relative wind vertical cross sections from the (left) graupel and (right) no-graupel simulations at (a),(b) 0235; (c),(d) 0310; and (e),(f) 0445 from cross-sectional lines shown in Fig. 9. Contour values identical to Fig. 4.

crystals in the no-graupel simulation. The low pressure perturbation associated with the graupel system had shifted farther rearward of the convective line (Fig. 13c). The convective updraft was still tilted over approximately 20 km, but it remained strong (Fig. 14b).

By 0445, the size of the graupel system convective updraft had diminished (Fig. 13e), although peak values remained steady (Fig. 14b). Concentrations of graupel aloft in the stratiform region were much lower as they continued to fall out of the stratiform updraft (Fig. 10e). The resulting melting and evaporation rates were lower (Fig. 11e) and the cold pool intensity had lessened

(Fig. 14a). Also evident was a weaker low pressure region, still approximately 25 km behind the convective line (Fig. 13e). The rear-to-front flow had descended to the surface even farther rearward of the convective line (Fig. 12e), the convective updraft was strongly tilted, and the system was weakening (Figs. 14b,c).

The no-graupel system still had large amounts of snow aloft (Fig. 10f). While a portion of the snow had fallen out, a significant amount remained, resulting in still-intense melting and evaporation rates throughout the entire wide system below the melting level (Fig. 11f). The cold pool of the no-graupel system was more

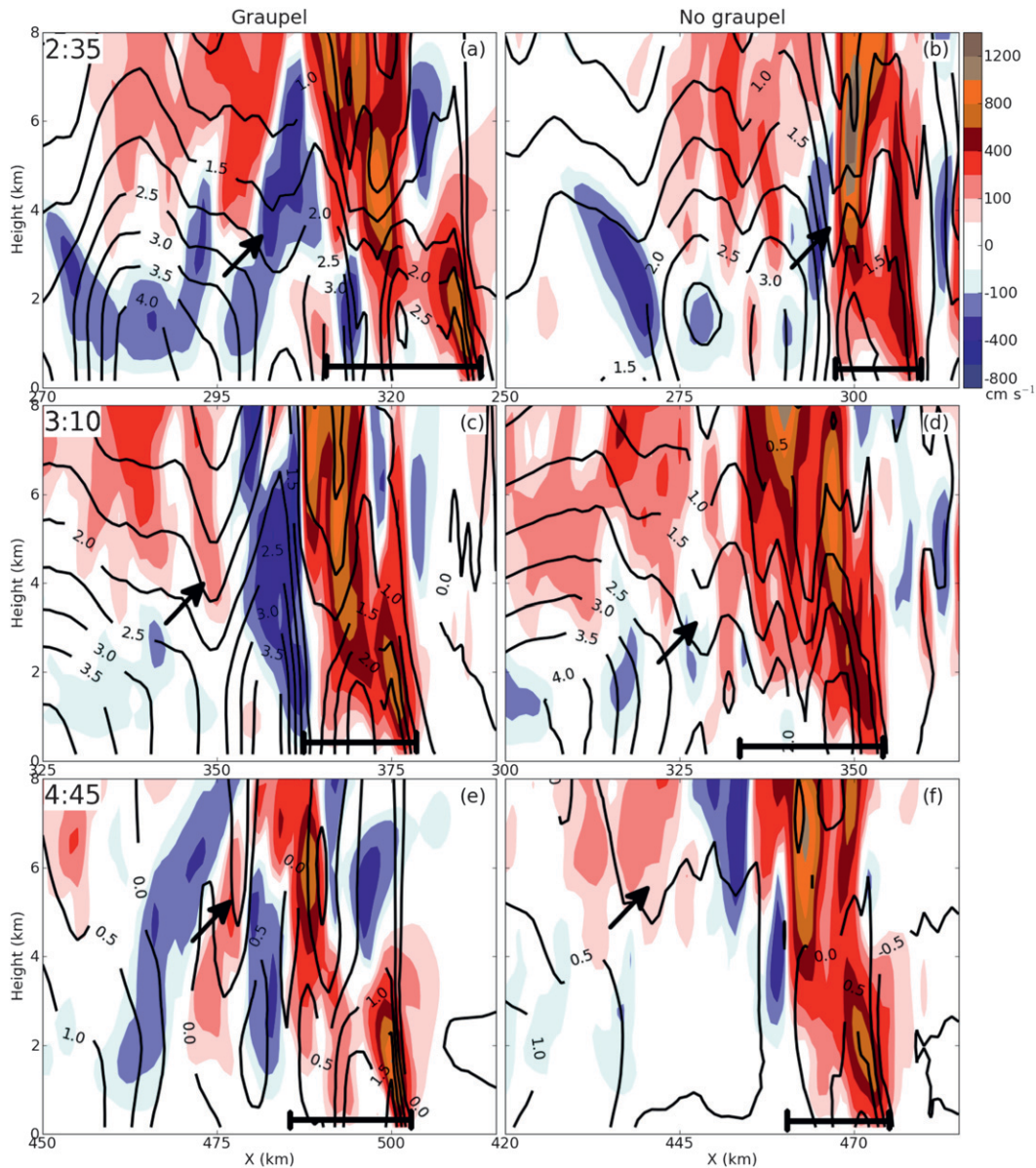


FIG. 13. Vertical motion and relative pressure perturbation cross-sections from the (left) graupel and (right) no-graupel case study simulation at (a),(b) 0235; (c),(d) 0310; and (e),(f) 0445. Perturbation pressure was calculated by subtracting the mean domain pressure profile from the total pressure field. Contour values, arrows, and brackets are identical to Fig. 7. These cross sections are a 65-km subset of the cross sections shown in Fig. 10.

intense than the graupel system's through the end of the simulation, although convective updraft and downdraft maxima of the two simulations were roughly steady through this period (Figs. 14a–c).

In summary, the no-graupel simulation cold pool transitioned from relatively warmer to cooler as the slower-falling snow finally began to melt; the system itself became more organized with stronger rear-to-front flow and bowing development as the simulation progressed. Meanwhile the graupel simulation cold pool

was intense from shortly after initialization, due to the large cooling rates produced by melting graupel and evaporating rain spread throughout the lower levels. However, the cooling rates lessened as the faster-falling graupel fell out of the storm; the strongly tilted updraft was unable to transport enough condensate aloft in replacement. Therefore, the graupel system began to weaken more quickly than the no-graupel simulation, as measured by total condensate aloft and cold pool intensity.

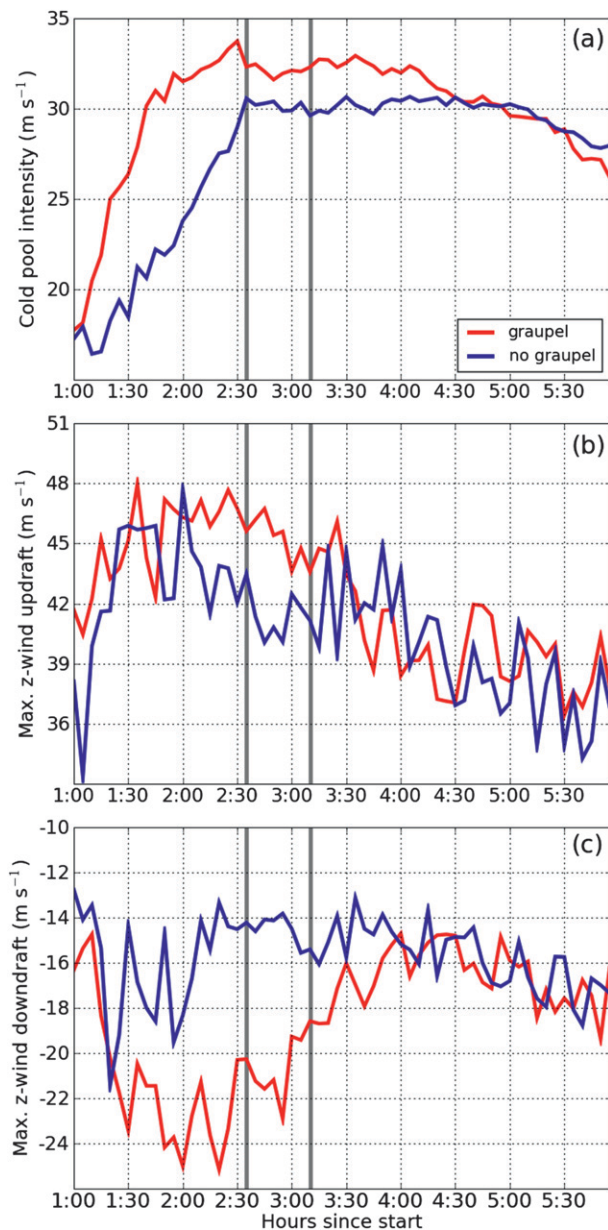


FIG. 14. Comparison of no-graupel (blue) and graupel (red) simulations from 1- to 6-h simulation time. (a) Maximum cold pool intensity ( $C$ ,  $\text{m s}^{-1}$ ), (b) maximum  $z$ -wind updraft ( $\text{m s}^{-1}$ ), and (c) maximum  $z$ -wind downdraft ( $\text{m s}^{-1}$ ). Maximum and minimum values are calculated over 5-min intervals over the entire domain. The two thick gray lines are the times new bowing development initiates in the no-graupel and graupel simulations (0235 and 0310, respectively).

## 5. Conclusions

This paper examines the effect of changes in microphysical cooling rates on bow echo generation, specifically through the connections among cold pool strength, rear-to-front flow, and convective updraft tilt. Multiple

WRF simulations were performed over a spectrum of graupel class parameters in a microphysical parameterization scheme, in order to directly and consistently vary the microphysical heating and cooling rates. The graupel parameter variations acted to render the class larger, more dense and “hail like,” or smaller, lighter, and “graupel like.” Additional simulations looked at the effects of removing graupel completely.

The simulations with a larger, more dense hail-like graupel class had these hydrometeors fall out of the updraft almost immediately, close to the convective line, allowing for little melting or evaporation. This resulted in a minimal stratiform precipitation region and reduced convective intensity. The system was less favorable to new bowing development, producing rear-to-front flow that did not descend to the surface until shortly before the convective line, and an updraft, which remained minimally tilted throughout.

The simulations with a smaller, less dense graupel-like graupel class had smaller graupel hydrometeors that were slower to fall, creating a wide stratiform precipitation region. This allowed for more melting and evaporation, and yielded a wider, deeper, and stronger cold pool. The rear-to-front flow descended to the surface quite some distance behind the convective line, aiding farther rearward tilt of the updraft. This helped generate bowing segments earlier than in the hail-like simulations.

A sensitivity test with smaller graupel-like hydrometeors that fell at the same speed as hail-like hydrometeors showed that their small mean size produced higher latent cooling rates, despite the decreased in-storm residence time. The faster fall speeds concentrated this cooling close to the convective line by allowing little advection, thereby creating an intense cold pool, surface-based rear-to-front flow, and faster new bowing development.

The various cloud and ice particles generated by the no-graupel (5 class) simulation remained almost entirely aloft for some time after initiation as the large amounts of snow generated fell slowly. Some time was required for the snow to reach the melting level. Until that point the melting and evaporation rates were minimal, and the cold pool initially not as intense as the “graupel” simulation (6 class). The resulting midlevel pressure perturbation and rear-to-front flow were weaker as well. Over time the cooling due to melting and evaporation increased as snow reached lower levels, forcing earlier descent of the rear-to-front flow to the surface and temporarily tilting the convective updraft, thus developing a bow echo.

The graupel simulation initially developed a stronger cold pool, as the faster-falling graupel hydrometeors

more quickly reached the melting level. The stronger cold pool and stronger, surface-based rear-to-front flow resulted in bowing developing faster. However, as the simulation progressed the vorticity associated with the cold pool and surface-based rear-to-front flow greatly overwhelmed that produced by the environmental shear, and the updraft weakened. The “no graupel” system eventually “caught up” to the graupel system’s intensity, as measured by cold pool intensity and updraft and downdraft strength.

Thus, it was found that internal variations in a WRF single-moment microphysics scheme, specifically regarding the graupel class, had a large effect on the development, strength, and structure of the simulated bowing convective system. Changes in the microphysical cooling rates affected the tilt of the convective updraft and development of rear-to-front flow, thereby affecting the timing, size, and existence of bowing.

The similarity of these results to those obtained by Weisman (1993), which used simulations with no ice, is noted. It is evident that frozen hydrometeors and their associated microphysical processes are not required for bowing development. However, in the simulations presented here it was found that the cooling produced by melting, and subsequently, evaporation, can play a significant role in creating a cold pool strong enough to initiate bowing. A delay in the onset of cooling by melting, as in the no-graupel simulation, helped the system retain a more upright updraft for a longer period of time. Extremely weak melting rates, such as in the hail-like case, resulted in systems with less intense cold pools and rear-to-front flow that bowed later. It is possible in real-time simulations that these results would be amplified as initiating mechanisms would not be as forceful as the “cold pool–dam break” method used in this study.

Furthermore, the variations in the horizontal distribution of the frozen hydrometeors, achieved by varying parameterization class size, had additional consequences. These effectively varied the horizontal scale and intensity of the cold pool, the location and strength of the midlevel pressure region, the rear-to-front flow, and the tilt of the convective updraft at the leading edge of the system. Thus, the impacts of frozen hydrometeors should not be discounted in future bowing simulations.

While this study has examined sensitivities to model microphysical schemes, such variations to the microphysics can occur in reality. For example, the introduction of dust into a system can drastically modify the concentration of both cloud condensation and ice-forming nuclei, as was seen in Twohy et al. (2010). This naturally results in significantly different size distributions of all hydrometeors in deep convection (van den

Heever et al. 2006; Storer et al. 2010); this particularly affects the heating and cooling rates as discussed here. There are many further environmental factors that could result in similar microphysical changes, such as variations in nearby temperature, moisture, or shear profiles. Changes in these profiles have been shown to primarily affect system circulation by modifying the internal system thermal forcing (Pandya and Durran 1996; Pandya et al. 2000), so these results are of note. Future work will include comparing systems produced by these microphysics scheme variations to observations.

*Acknowledgments.* This research was supported by National Science Foundation Grant ATM-0500061, and conducted under the Cooperative Research Data Agreement between the Air Force Weather Agency and Atmospheric Environmental Research, Inc. Susan van den Heever is supported by the NSF under Grant ATM-0820557. Computing resources were provided by the Navy Department of Defense Supercomputing Resource Center (Navy DSRC) and the Army Research Laboratory Department of Defense Supercomputing Resource Center (ARL DSRC), which are sponsored by the DoD High Performance Computing Modernization Program. The authors thank Morris Weisman, George Bryan, and Kevin Manning of NCAR, and Steven Rutledge of CSU, for discussions regarding this work and assistance in using the WRF model. The comments of three anonymous reviewers were also of great help.

#### REFERENCES

- Biggerstaff, M. I., and R. A. Houze, 1991: Kinematic and precipitation structure of the 10–11 June 1985 squall line. *Mon. Wea. Rev.*, **119**, 3034–3065.
- , and —, 1993: Kinematics and microphysics of the transition zone of the 10–11 June 1985 squall line. *J. Atmos. Sci.*, **50**, 3091–3110.
- Bryan, G. H., and H. Morrison, 2012: Sensitivity of a simulated squall line to horizontal resolution and parameterization of microphysics. *Mon. Wea. Rev.*, **140**, 202–225.
- , J. C. Knievel, and M. D. Parker, 2006: A multimodel assessment of RKW theory’s relevance to squall-line characteristics. *Mon. Wea. Rev.*, **134**, 2772–2792.
- Chen, S., and W. R. Cotton, 1988: The sensitivity of a simulated extratropical mesoscale convective system to longwave radiation and ice-phase microphysics. *J. Atmos. Sci.*, **45**, 3897–3910.
- Cheng, L., M. English, and R. Wong, 1985: Hailstone size distributions and their relationship to storm thermodynamics. *J. Climate Appl. Meteor.*, **24**, 1059–1067.
- Cohen, C., and E. W. McCaul Jr., 2006: The sensitivity of simulated convective storms to variations in prescribed single-moment microphysics parameters that describe particle distributions, sizes, and numbers. *Mon. Wea. Rev.*, **134**, 2547–2565.
- Dawson, D. T., II, M. Xue, J. A. Milbrandt, and M. K. Yau, 2010: Comparison of evaporation and cold pool development between single-moment and multimoment bulk microphysics

- schemes in idealized simulations of tornadic thunderstorms. *Mon. Wea. Rev.*, **138**, 1152–1171.
- Dennis, A. S., P. L. Smith Jr., G. A. P. Peterson, and R. D. McNeil, 1971: Hailstone size distributions and equivalent radar reflectivity factors computed from hailstone momentum records. *J. Appl. Meteor.*, **10**, 79–85.
- Federer, B., and A. Waldvogel, 1975: Hail and raindrop size distributions from a Swiss multicell storm. *J. Appl. Meteor.*, **14**, 91–97.
- Fovell, R. G., and Y. Ogura, 1988: Numerical simulation of a mid-latitude squall line in two dimensions. *J. Atmos. Sci.*, **45**, 3846–3879.
- , and —, 1989: Effect of vertical wind shear on numerically simulated multicell storm structure. *J. Atmos. Sci.*, **46**, 3144–3176.
- Garner, S. T., and A. J. Thorpe, 1992: The development of organized convection in a simplified squall-line model. *Quart. J. Roy. Meteor. Soc.*, **118**, 101–124.
- Gilmore, M. S., J. M. Straka, and E. N. Rasmussen, 2004a: Precipitation uncertainty due to variations in precipitation particle parameters within a simple microphysics scheme. *Mon. Wea. Rev.*, **132**, 2610–2627.
- , —, and —, 2004b: Precipitation and evolution sensitivity in simulated deep convective storms: Comparisons between liquid-only and simple ice and liquid phase microphysics. *Mon. Wea. Rev.*, **132**, 1897–1916.
- Hane, C. E., 1973: The squall line thunderstorm: Numerical experimentation. *J. Atmos. Sci.*, **30**, 1672–1690.
- Hong, S. Y., and J. O. J. Lim, 2006: The WRF single-moment 6-class microphysics scheme (WSM6). *J. Korean Meteor. Soc.*, **42**, 129–151.
- , J. Dudhia, and S. H. Chen, 2004: A revised approach to ice microphysical processes for the bulk parameterization of clouds and precipitation. *Mon. Wea. Rev.*, **132**, 103–120.
- , K. S. Sunny Lim, J. H. Kim, J. O. Jade Lim, and J. Dudhia, 2009: Sensitivity study of cloud-resolving convective simulations with WRF using two bulk microphysical parameterizations: Ice-phase microphysics versus sedimentation effects. *J. Appl. Meteor. Climatol.*, **48**, 61–76.
- James, R. P., J. M. Fritsch, and P. M. Markowski, 2006: Bow echo sensitivity to ambient moisture and cold pool strength. *Mon. Wea. Rev.*, **134**, 950–963.
- Knight, C. A., W. A. Cooper, D. W. Breed, I. R. Paluch, P. L. Smith, and G. Valie, 1982: Microphysics. *Hailstorms of the Central High Plains*, C. Knight and P. Squires, Eds., Vol. 1, Colorado Associated University Press, 151–193.
- Lafore, J. P., and M. W. Moncrieff, 1989: A numerical investigation of the organization and interaction of the convective and stratiform regions of tropical squall lines. *J. Atmos. Sci.*, **46**, 521–544.
- Lerach, D. G., B. J. Gaudet, and W. R. Cotton, 2008: Idealized simulations of aerosol influences on tornadogenesis. *Geophys. Res. Lett.*, **35**, L23806, doi:10.1029/2008GL035617.
- Lim, K. S. S., and S. Y. Hong, 2010: Development of an effective double-moment cloud microphysics scheme with prognostic cloud condensation nuclei (CCN) for weather and climate models. *Mon. Wea. Rev.*, **138**, 1587–1612.
- Lin, Y. L., R. D. Farley, and H. D. Orville, 1983: Bulk parameterization of the snow field in a cloud model. *J. Climate Appl. Meteor.*, **22**, 1065–1092.
- Marshall, J. S., and W. Mc K. Palmer, 1948: The distribution of raindrops with size. *J. Meteor.*, **5**, 165–166.
- Morrison, H., and J. Milbrandt, 2011: Comparison of two-moment bulk microphysics schemes in idealized supercell thunderstorm simulations. *Mon. Wea. Rev.*, **139**, 1103–1130.
- , G. Thompson, and V. Tatarskii, 2009: Impact of cloud microphysics on the development of trailing stratiform precipitation in a simulated squall line: Comparison of one- and two-moment schemes. *Mon. Wea. Rev.*, **137**, 991–1007.
- Nicholls, M. E., 1987: A comparison of the results of a two-dimensional numerical simulation of a tropical squall line with observations. *Mon. Wea. Rev.*, **115**, 3055–3077.
- , R. H. Johnson, and W. R. Cotton, 1988: The sensitivity of two-dimensional simulations of tropical squall lines to environmental profiles. *J. Atmos. Sci.*, **45**, 3625–3649.
- Pandya, R. E., and D. R. Durran, 1996: The influence of convectively generated thermal forcing on the mesoscale circulation around squall lines. *J. Atmos. Sci.*, **53**, 2924–2951.
- , —, and M. L. Weisman, 2000: The influence of convective thermal forcing on the three-dimensional circulation around squall lines. *J. Atmos. Sci.*, **57**, 29–45.
- Parker, M. D., 2010: Relationship between system slope and updraft intensity in squall lines. *Mon. Wea. Rev.*, **138**, 3572–3578.
- Pruppacher, H. R., and J. D. Klett, 1978: *Microphysics of Clouds and Precipitation*. D. Reidel, 714 pp.
- Rotunno, R., J. B. Klemp, and M. L. Weisman, 1988: A theory for strong, long-lived squall lines. *J. Atmos. Sci.*, **45**, 463–485.
- Rutledge, S. A., and P. V. Hobbs, 1983: The mesoscale and microscale structure and organization of clouds and precipitation in mid-latitude cyclones. Part VIII: A model for the “seeder feeder” process in warm-frontal rainbands. *J. Atmos. Sci.*, **40**, 1185–1206.
- Seigel, R. B., and S. C. van den Heever, 2013: Squall-line intensification via hydrometeor recirculation. *J. Atmos. Sci.*, in press.
- Skamarock, W. C., and Coauthors, 2008: A description of the Advanced Research WRF Version 3. NCAR Tech. Note NCAR/TN-475+STR, 113 pp.
- Snook, N. A., and M. Xue, 2008: Effects of microphysical drop size distribution on tornadogenesis in supercell thunderstorms. *Geophys. Res. Lett.*, **35**, L24803, doi:10.1029/2008GL035866.
- Spahn, J. E., 1976: The airborne hail disdrometer: An analysis of its 1975 performance. Rep. 76-13, Institute of Atmospheric Sciences, South Dakota School of Mines and Technology, Rapid City, SD, 65 pp.
- Stensrud, D. J., M. C. Coniglio, R. P. Davies-Jones, and J. S. Evans, 2005: Comments on “‘A theory for strong long-lived squall lines’ revisited.” *J. Atmos. Sci.*, **62**, 2989–2996.
- Stoelinga, M. T., 2005: Simulated equivalent reflectivity factor as currently formulated in RIP: Description and possible improvements. Read/Interpolate/Plot Implementation Document, 5 pp. [Available online at [http://www.atmos.washington.edu/~stoeling/RIP\\_sim\\_ref.pdf](http://www.atmos.washington.edu/~stoeling/RIP_sim_ref.pdf).]
- Storer, R. L., S. C. van den Heever, and G. L. Stephens, 2010: Modeling aerosol impacts on convective storms in different environments. *J. Atmos. Sci.*, **67**, 3904–3915.
- Szeto, K., and H. Cho, 1994: A numerical investigation of squall lines. Part III: Sensitivity to precipitation processes and the Coriolis force. *J. Atmos. Sci.*, **51**, 1341–1351.
- Tao, W. K., and J. Simpson, 1989: Modeling study of a tropical squall-type convective line. *J. Atmos. Sci.*, **46**, 177–202.
- Thorpe, A. J., M. J. Miller, and M. W. Moncrieff, 1982: Two-dimensional convection in non-constant shear: A model of mid-latitude squall lines. *Quart. J. Roy. Meteor. Soc.*, **108**, 739–762.
- Twohy, C. H., and Coauthors, 2010: Relationships of biomass-burning aerosols to ice in orographic wave clouds. *J. Atmos. Sci.*, **67**, 2437–2450.
- van den Heever, S. C., and W. R. Cotton, 2004: The impact of hail size on simulated supercell storms. *J. Atmos. Sci.*, **61**, 1596–1609.

- , and —, 2007: Urban aerosol impacts on downwind convective storms. *J. Appl. Meteor. Climatol.*, **46**, 828–850.
- , G. G. Carrió, W. R. Cotton, P. J. DeMott, and A. J. Prenni, 2006: Impacts of nucleating aerosol on Florida storms. Part I: Mesoscale simulations. *J. Atmos. Sci.*, **63**, 1752–1775.
- van Weverberg, K., N. P. M. van Lipzig, and L. Delobbe, 2011: The impact of size distribution assumptions in a bulk one-moment microphysics scheme on simulated surface precipitation and storm dynamics during a low-topped supercell case in Belgium. *Mon. Wea. Rev.*, **139**, 1131–1147.
- , —, —, and A. M. Vogelmann, 2012a: The role of precipitation size distributions in km-scale NWP simulations of intense precipitation: Evaluation of cloud properties and surface precipitation. *Quart. J. Roy. Meteor. Soc.*, **138**, 2163–2181.
- , A. M. Vogelmann, H. Morrison, and J. Milbrandt, 2012b: Sensitivity of idealized squall-line simulations to the level of complexity used in two-moment bulk microphysics schemes. *Mon. Wea. Rev.*, **140**, 1883–1907.
- Weisman, M. L., 1992: The role of convectively generated rear-inflow jets in the evolution of long-lived mesoconvective systems. *J. Atmos. Sci.*, **49**, 1826–1847.
- , 1993: The genesis of severe long-lived bow echoes. *J. Atmos. Sci.*, **50**, 645–670.
- , and R. Rotunno, 2004: “A theory for strong long-lived squall lines” revisited. *J. Atmos. Sci.*, **61**, 361–382.
- , and —, 2005: Reply. *J. Atmos. Sci.*, **62**, 2997–3002.
- , W. C. Skamarock, and J. B. Klemp, 1997: The resolution dependence of explicitly modeled convective systems. *Mon. Wea. Rev.*, **125**, 527–548.
- Yang, M. J., and R. A. Houze Jr., 1995: Sensitivity of squall-line rear inflow to ice microphysics and environmental humidity. *Mon. Wea. Rev.*, **123**, 3175–3193.